Available online at www.sciencedirect.com

ScienceDirect

Journal of Magnesium and Alloys 10 (2022) 915–937

www.elsevier.com/locate/jma

Review

Laser additive manufacturing of biodegradable Mg-based alloys for biomedical applications: A review

C.L. Wu, W.J. Xie, H.C. Man*

Department of Industrial and Systems Engineering, The Hong Kong Polytechnic University, Hung Hom, Kowloon, Hong Kong, China

Received 29 September 2021; received in revised form 3 December 2021; accepted 27 December 2021
Available online 2 March 2022

Abstract

Metallic implants are widely used in internal fixation of bone fracture in surgical treatment. They are mainly used for providing mechanical support and stability during bone reunion, which usually takes a few months to complete. Conventional implants made of stainless steels, Ti-based alloys and CoCrMo alloys have been widely used for orthopedic reconstruction due to their high strength and high corrosion resistance. Such metallic implants will remain permanently inside the body after implantation, and a second surgery after bone healing is needed because the long-term presence of implant will lead to various problems. An implant removal surgery not only incurs expenditure, but also risk and psychological burden. As a consequence, studies on the development of biodegradable implants, which would degrade and disappear *in vivo* after bone reunion is completed, have drawn researchers' attention. In this connection, Mg-based alloys have shown great potentials as promising implant materials mainly due to their low density, inherent biocompatibility, biodegradability and mechanical properties close to those of bone. However, the high degradation rate of Mg-based implants *in vivo* is the biggest hurdle to overcome. Apart from materials selection, a fixation implant is ideally tailor-made in size and shape for an individual case, for best surgical outcomes. Therefore, laser additive manufacturing (LAM), with the advent of sophisticated laser systems and software, is an ideal process to solve these problems. In this paper, we reviewed the progress in LAM of biodegradable Mg-based alloys for biomedical applications. The effect of powder properties and laser processing parameter on the formability and quality was thoroughly discussed. The microstructure, phase constituents and metallurgical defects formed in the LAMed samples were delineated. The mechanical properties, corrosion resistance, biocompatibility and antibacterial properties of the LAMed samples were summarized and compared with samples fabricated by traditional processes. In addition, we have made some suggestions for advancing the knowledge in the LAM of Mg-based alloys for biomedical implants.

Keywords: Laser additive manufacturing; Magnesium alloys; Implant; Biomedical applications; Mechanical properties; Biodegradability.

1. Introduction

Conventional implants made of stainless steel, Ti-based alloys and CoCrMo alloys, which have been widely used in orthopedic applications, will remain permanently inside the body after implantation [1–6]. Generally, these permanent alloys suffer from two major drawbacks, one being biological and the other mechanical. For example, stainless steel suffers from pitting corrosion and subsequent release of allergenic/toxic Ni and Cr ions in body fluids. The discharge of these harmful ions can activate undesirable inflammatory and immune reactions in the human body, which becomes the main drawbacks in long-term usage in biological environments [3,4]. For Ti6Al4V, the Al ion released may inhibit bone growth and may even potentially lead to Alzheimer's disease [2]. In addition, V ion and its oxide (V_2O_5) are known to be cytotoxic. These will constitute a potential threat to its safe use *in vivo* [5]. On the other hand, CoCrMo implants may release cobalt and chromium ions, which may induce cytotoxicity, DNA damage, metal hypersensitivity reactions and pseudotumors [6]. In conclusion, these conventional alloys in medical applications inevitably contain biologically toxic elements such as Al, Ni, Cr, V, etc. Beside the bio-

* Corresponding author.
E-mail address: hc.man@polyu.edu.hk (H.C. Man).

https://doi.org/10.1016/j.jma.2021.12.014

logical concern of these conventional alloys, their mechanical compatibility is another problematic issue. These alloys possess a Young's modulus much higher than that of the human cortical bone, which would cause stress-shielding. In general, an invasive second surgery is usually required to remove the implants after bone reunion is complete. In view of these inherent inadequacies of conventional metallic materials, biodegradable implants have drawn researchers' attention over the past decades, which might circumvent the disadvantage of permanent implants. Biodegradable implants are expected to provide and maintain mechanical support and stability for bone reunion during the first few months. Once bone reunion is completed, the implant would degrade and disappear *in vivo*, thus avoiding a second surgery for implant removal. In fact, polymeric materials including polylactic-co-glycolic and polylactic acid have been used as biodegradable implants for internal fixation in orthopedics [7,8]. However, such implants are only used in low loading-bearing applications due to the low strength of polymeric materials. Metallic biodegradable implants, as a new generation of metal implants, are supposed to support the damaged tissue with a slow corrosion rate in the human body, and then degrade completely after recovery of the damaged tissue. Metallic implants are more suitable for orthopedic implants requiring high strength and toughness, which are not possessed by polymeric implants. Among various biodegradable metallic materials, Fe-based, Zn-based and Mg-based alloys are potential candidate metallic materials as these materials are all nontoxic and biodegradable with different rates [9–11]. It is well-known that maintaining the mechanical integrity during the healing period is important for the degradable implants. Mg- and Fe-based implants possess excellent mechanical properties, while the low degradable rate of Fe-based implants restricts applications in biodegradable implant. In addition, harmful metal ions generated from corrosion can result in inflammation, cell apoptosis and other destructive tissue reactions. Meanwhile, the Young's modulus of Fe-based and Zn-based implants is much higher than that of natural bone. Among these biodegradable metallic materials, Mg-based alloys are the most intensively studied materials in orthopedic applications on account of their inherent biocompatibility, biodegradability, desirable Young's modulus [12–14]. Mg-based alloys possess a density of ~1.79 g/cm^3, which is similar to that of human bone (1.75 g/cm^3). Its Young's modulus is approximately 45 GPa, whereas that of Ti-based and 316 L stainless steel are 110 and 193 GPa, respectively. Thus the Young's modulus of Mg-based alloys is closest to that of the natural bone (10–27 GPa) among the metallic materials and can effectively minimize the shielding effect due to mismatch of the Young's modulus between implant and natural bone. In addition, Mg ion is the fourth most prevalent mineral in the human body and also one of the important factors for bone metabolism, which exerts a great influence on bone osteoclast and induces the formation of apatite [15]. It was reported that 21–28 g of Mg is required for a healthy adult to maintain regular functions, and 250–350 mg of Mg is recommended for daily allowance [16]. In summary, Mg-based alloys show great potentials for applications in biodegradable orthopedic implants. However, Mg-based alloys suffer from a high corrosion rate in physiological environments [17,18]. Bone recovery generally goes through three periods such as inflammation, repair and reconstruction. Biodegradable Mg-based alloys are supposed to offer enough support to protect the fracture site from the secondary damage at the period of inflammation and repair. Hence, a relatively low corrosion rate is required for the Mg-based implants to provide adequate load-bearing function. In addition to a high corrosion rate, Mg-based alloys exhibit a poor cold workability as the dislocation slip only takes place on the (0001) basal plane and the <11_20> direction, or the (10_12) pyramidal plane for the twinning at room temperature [19,20]. As a consequence, Mg-based alloys parts are usually produced by deformation processing at elevated temperature, aiming at activating more slip systems to allow better formability [21,22]. This would result in the oxidation of the samples, deterioration of surface quality and decrease of processing efficiency. Chen et al [23]. thoroughly investigated the effect of heat treatment on mechanical and biodegradable properties of an extruded ZK60 alloy. This research revealed that the sample with T5 treatment exhibited improved mechanical properties and degradation behavior because of the formation of small and uniformly distributed MgZn phases. On the other hand, the extruded sample and the sample with T6 treatment suffered from serious corrosion owing to the formation of second phases, leading to serious galvanic corrosion. Sun et al [24]. studied the mechanical properties, degradable behavior and cytotoxicity of a new biomedical Mg-Zn-Ca alloy prepared by extrusion. It is found that the peak strength, yield strength, elongation and elastic modulus of the extruded Mg-4.0Zn-0.2Ca alloy were 297 MPa, 240 MPa, 21.3% and 45 GPa, respectively, but decreased to 160 MPa, 220 MPa, 8.5% and 40 GPa after 30 days immersion in simulated body fluid. Song et al [25]. explored the effect of precipitated phases on the corrosion behavior of Mg-5 Zn alloy. It is reported that the T4-treated sample possessed the highest corrosion resistance due to the absence of precipitated phases, while the T6-treated sample was the worst one due to the formation of precipitated phases, which acted as micro-cathodes to accelerate corrosion. Until now, most of the Mg-based alloys are still prepared by casting due to a higher processing efficiency and precision. However, this processing route is not suitable for parts with complex geometric shape like that of implants. In addition, the properties of samples often deteriorate because thermodynamically stable phases might be formed during solidification and it is difficult to control the distribution or morphology of the precipitated phase. Wei et al [26]. investigated the effect of Zn content on the corrosion resistance of Mg-*x*Zn-0.2Ca-0.1Mn alloys prepared by casting. It is found that precipitated phases such as $Ca_2Mg_6Zn_3$, Mg_2Ca and Mg_4Zn_7 were formed but the microstructure was obviously refined with the increase of Zn content. In addition, the corrosion resistance was first increased and then decreased with the addition of Zn. The Mg-1Zn-0.1Mn-0.2Ca alloy exhibited the highest corrosion resistance, with a corrosion rate of 6.09 mm/y. Zhang et al [27]. studied the corrosion behavior and biocompatibility of

Mg-Zn-Mn alloys prepared by casting for biomedical applications. This work revealed that Zn can contribute to the formation of passivation film and thus protect the Mg-based alloys from corrosion damage in simulated body fluids. Moreover, the Mg-based alloys exhibited excellent cytocompatibility as demonstrated by cell culture and hemolysis tests.

Laser additive manufacturing (LAM), is a promising candidate to produce metal prototypes using metal-based powders, which has the advantage of directly building near net shaped and complexly formed component parts via computer aided design data without using any molds or tools. In addition, LAM is characterized by rapid melting/solidification with a cooling rate of above 10^5 K/s, which contributes to the extended solubility of alloying elements, refining of grain size and formation of a more homogeneous microstructure [28–32]. Many researchers have reported that the corrosion resistance of Mg-based alloys with refined grains was much better than that of the alloys with coarse grain. The extended solubility of alloying elements can effectively inhibit the formation of precipitated phases and thus protect the Mg-based alloys from galvanic corrosion. Moreover, a homogeneous microstructure resulting from the strong Marangoni convection and the following solution capture effect during LAM would reduce pit corrosion tendency as segregation is minimized. Li et al [33]. revealed that extruded Mg-1Ca alloy with refined grains exhibited a lower hydrogen evolution rate than cast Mg-1Ca during immersion tests, and the surface film on the former was more protective than that on the later. Gu et al [34]. and Shuai et al [35]. also found that extruded and LAMed Mg-Zn-Zr alloys possessed an improved corrosion behavior in comparation with cast Mg-Zn-Zr. Argade et al [36]. thoroughly investigated the effect of grain size from 70 μm to 0.7 μm on the corrosion resistance of Mg-Y-RE alloys by electrochemical and immersion tests. This particular study showed that a decrease of one order in corrosion rate could be achieved for Mg-based alloys via grain refining.

Therefore, LAM of Mg-based alloys containing Al or RE are most widely to tailor fabricate Mg-based implants with a lower degradation rate that is difficult or impossible to achieve by conventional melting and deformation processing due to the limited cold workability resulting the close-packed hexagonal structure. Despite the rapid development of LAM technique, the process of LAM is mainly focused on Fe-based alloys, Ti-based alloys, Ni-based alloys and Al-based alloys [37–40], while studies on LAM of Mg-based alloys are less reported [35]. This can be attributed to difficulties including the insufficient fusion of powder, the high vapor pressure of Mg and the presence of large pores in the LAMed samples resulting from poor understanding of process control during laser-powder interaction and melting pool solidification. As a consequence, the current work aims to provide a comprehensive review of recent studies on LAM of biodegradable Mg-based alloys for biomedical applications.

2. Influence of powder properties and laser processing parameters on the formability of LAMed Mg-based alloys

2.1. Influence of powder properties on the formability of LAMed Mg-based alloys

LAM technique is an attractive and emerging process for tailor making metallic implants with complex geometric shape. However, some difficulties still need to be overcome in the LAM process for fabricating Mg-based parts. Metallurgical defects such as pores and low relative density are common in LAMed parts. The low formability can be attributed to improper processing parameters like under-heating and over-heating, leading to incomplete melting or vaporization. In addition, the quality of raw powders also plays an important role on the quality of the parts prepared by LAM. Therefore, the quality of raw powders and selection of processing parameters are of paramount importance in successful LAM fabrication. Ng et al [41]. carried out single-track melting of two grades of Mg powders using a self-developed LAM system in an atmosphere of high-purity argon Fig. 1. shows the SEM micrograph of two grades of Mg powders. It is noticed that these two grades of Mg powders one was irregularly shaped with size between 75 and 150 μm (Fig. 1(a)) and the other was spherically shaped with size between 5 and 45 μm (Fig. 1(b)).

Figure 2 shows macro morphology of single-track melting samples using these Mg powders. It was reported that the irregular and coarse Mg powders could not melt or be sintered (Fig. 2(a)), while successful melting of single-track of Mg was obtained using the spherical fine powder (Fig. 2(b)). This phenomenon indicates that spherical and fine powder would tend to form smooth and compact tracks by LAM.

In addition, Hu et al [42]. investigated the effect of powder size on the formability of LAMed magnesium Fig. 3. shows the macro-morphology of LAMed magnesium using different powder size. They reported that the groove perpendicular to the spreading direction appeared at the starting edge of LAMed sample using 25 μm powder, and Wang et al [43]. also observed a similar phenomenon in LAM of 316 stainless steel. The magnesium powders were irradiated for a longer time as the scanning velocity of laser was low at the starting edge of samples. Therefore, more Mg powders were absorbed into the melting pool, leading to the formation of groove near the protuberance edge. However, no grooves were formed in the LAMed sample using 43 μm powder. This phenomenon can be attributed to the fact that the melting pool life was affected by powder size. In addition, the coarse powders may not be absorbed by the melting as easily as the fine powder. The SEM topology as shown in Fig. 4 indicates that the LAMed sample using 25 μm powder exhibited a rough surface with many unmelted and spheroidised particles compared to the LAMed sample using 43 μm powder.

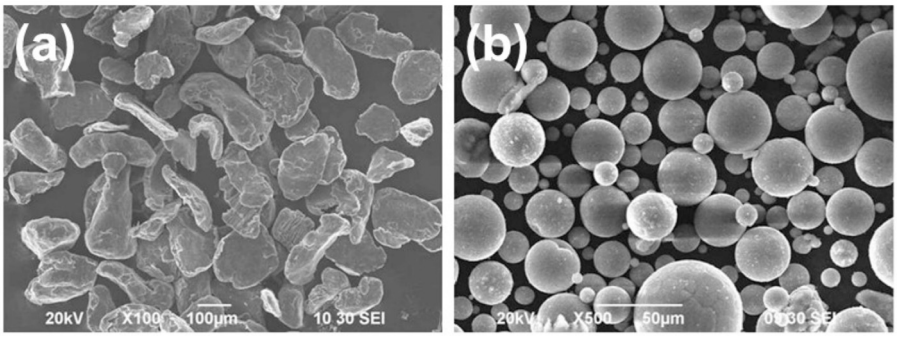

Fig. 1. SEM micrograph of irregular-shaped coarse Mg powders (a) and spherical-shaped fine Mg powders (b) [41].

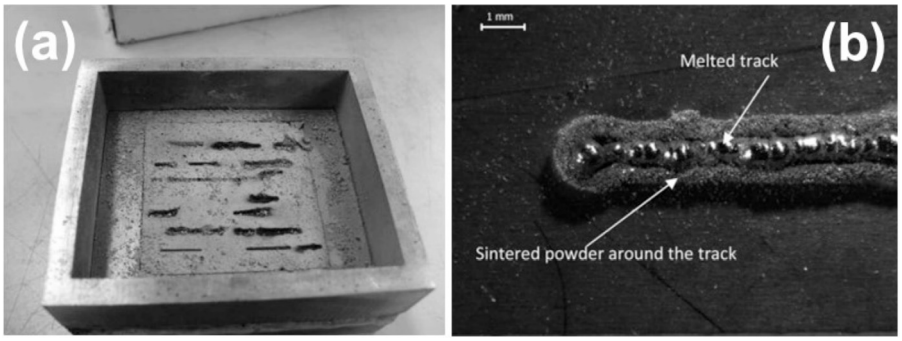

Fig. 2. Macro morphology of single-track melting samples using coarse Mg powders (a) and fine Mg powders (b) [41].

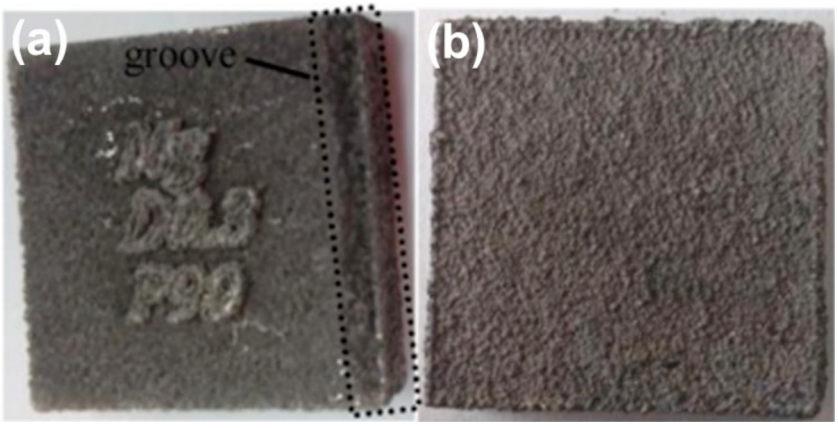

Fig. 3. Macro morphology of LAMed magnesium using different powder size. (a) 25.85 μm, (b) 43.32 μm [42].

2.2. *Influence of laser processing parameters on the formability of LAMed Mg-based alloys*

Beside the quality of raw powder used in LAM, most works focused on the effect of laser processing parameters on the formability, microstructure and properties, including laser input power, scanning velocity, scanning strategy, hatching distance, laser spot diameter or powder layer thickness Table 1. summarizes the processing parameters via LAM for manufacturing Mg-based alloys reported in the literature.

Wei et al [44]. investigated the effect of laser scanning velocity on the formability of LAMed Mg–Zn–Zr components. The macro morphology and relative density of as-built components are shown in Fig. 5. It was reported that element vaporization was very serious at a low scanning velocity of 100 mm/s, leading to the appearance of ablated pits on the sample surface. A high relative density of 94.05% could be achieved for samples obtained at a scanning velocity of 300 mm/s. However, further increasing the scanning velocity (500 mm/s, 700 mm/s and 900 mm/s) resulted in decrease of relative density to 82.25% owing to incomplete melting of the powders and hence internal pores in the sample.

Figure 6 shows the SEM image of LAMed Mg–9%Al samples surface with variation in process parameters. It is reported [55] that fine cauliflower-like grains appeared on the surface of metal bulk with interconnected pores (Fig. 6(a) and (b)), resulting from the metal evaporation–solidification process. Due to the low melting/boiling temperature, Mg powders

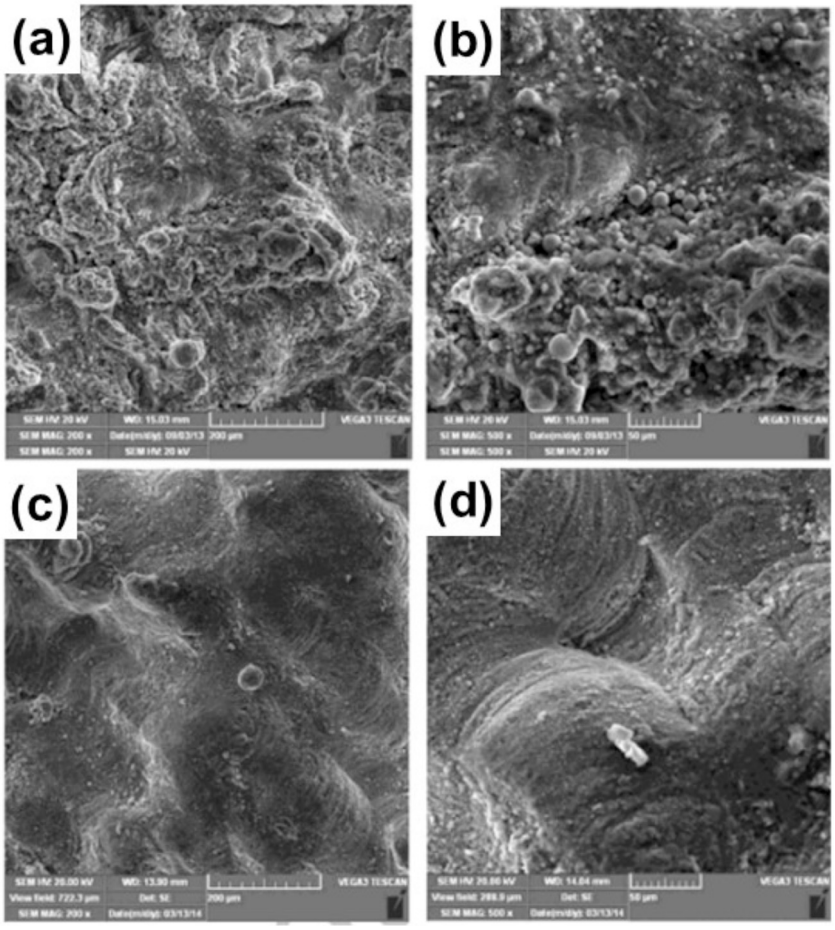

Fig. 4. SEM topology of LAMed magnesium using different powder size. (a) and (b) 25.85 μm, (c) and (d) 43.32 μm [42].

Table 1
Processing parameters in LAM for manufacturing Mg-based alloys.

Sample	Laser power (W)	Scanning speed (mm/s)	Spot size (μm)	Hatching distance (μm)	Layer thickness (μm)	Laser type
Mg–Zn–Zr [44]	200	100–900	150	80	20	Fiber
Mg-9wt%Al [45]	70	500–1250	80	30	30	Nd:YAG
ZK30-Cu [46]	75	15	150	50	50	–
ZK60-Cu [47]	60	10	150	100	–	Fiber
AZ91D [48]	200	167–1000	100	70–130	40	Fiber
Mg-RE [49]	4000	–	5000	–	400	CO2
Mg-Ca [50]	50–100	10	–	150	40	Nd:YAG
Mg-Zn [51]	180	700	150	70	20	Fiber
WE43 [52]	200	700	90	40	30	Fiber
Mg–*x*Al–Zn [53]	80	3	50	100	60	Fiber
AZ61 [54]	100	10	80	100	150	Fiber

can be easily heated above melting point and form melting pool during laser irradiation. In addition, the melting pool would absorb much more laser energy than that of powder layer, resulting in the increase of the melting pool temperature beyond the boiling point of Mg (1093 °C). Thus, the vapor pressure of Mg increased from 0.36 KPa at the melting point to 51 KPa at the boiling point.

Mg would evaporate and the surface of the melting pool was covered by the metal vapor. Fine cauliflower-like grains were formed when the Mg vapor deposited on the surface of the solid metal. It is noticed that balling phenomenon appeared on the samples obtained at the high scanning velocity as shown in (Fig. 6(c) and (d)), which can be attributed to the capillary instability of the liquid track. The high scanning velocity resulted in the increase of melting instability and small-sized liquid droplets tended to splash from the surface of the melting track owing to the decrease of the surface energy of the melt pool, leading to the appearance of balling.

In addition, a processing map based on the formability of Mg-based alloys was developed by Wu et al [56]. (Fig. 7).

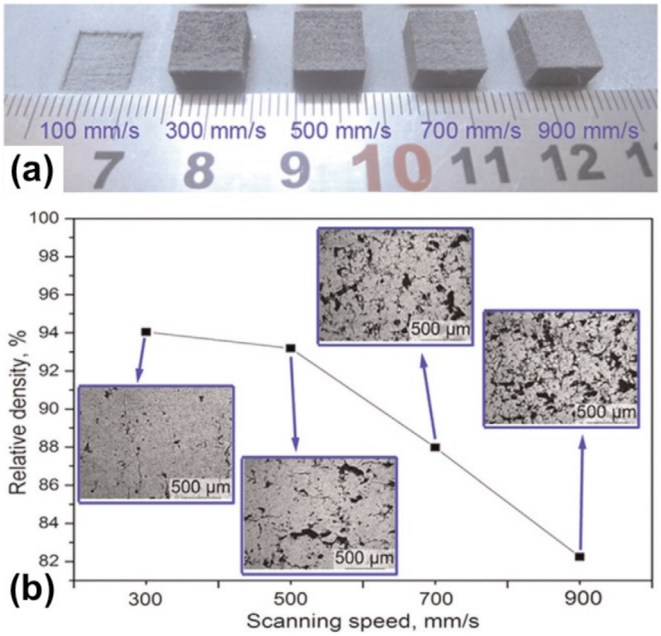

Fig. 5. Macro morphology and relatively density of LAMed Mg–Zn–Zr components [44].

According to the quality of LAMed samples, the overheating region (Region I and II), under-heating region (Region III and IV) and forming region (Region V) can be determined among within the test range of the laser input power and scanning speed. Samples with minimum porosity (approximately 2.0%) were obtained in the forming region (Fig. 8).

Among previous studies, laser energy density (E) is commonly used to control the formability of the LAMed samples. The laser energy density (E) can be the linear energy density, 2D energy density or 3D energy density, and is defined, respectively as [57]:

$$\text{linear energy density}: E = \frac{p}{v}\mathrm{j}\,m^{-1} \tag{1}$$

$$\text{2D energy density}: E = \frac{p}{v \times h} J\,m^{-2} \tag{2}$$

$$\text{3D energy density}: E = \frac{p}{v \times h \times t} J\,m^{-3} \tag{3}$$

where P is laser input power, v is laser scanning velocity, h is hatching distance and t is layer thickness. It is well known that a relatively low E supplied to the powder might result in insufficient melting or insufficient fusion between adjacent tracks or layers, leading to poor mechanical properties [58]. When E is relatively high, vigorous vaporization would occur due to the low boiling point and high vapor pressure of Mg, leading to the formation of pores and decrease of dimensional accuracy [44]. In addition, the keyhole effect would appear at high E (at high laser power and low scanning velocity), causing a deep melting pool with strong melting pool dynamics because the melting pool propagated forward and the vapor cavity collapsed [59]. The keyhole mode is one of the most important factors during the formation of pores and is a severe instability regime. The formation mechanism of keyhole mode porosity based on recoil pressure and surface tension was thoroughly investigated in a previous work [56] Fig. 9. shows the schematic diagram of keyhole mode porosity. It is noticed from Fig. 9(a) that due to the low boiling point and high vapor pressure of Mg, the temperature at the bottom of the keyholes could be above the evaporation point when the powders are

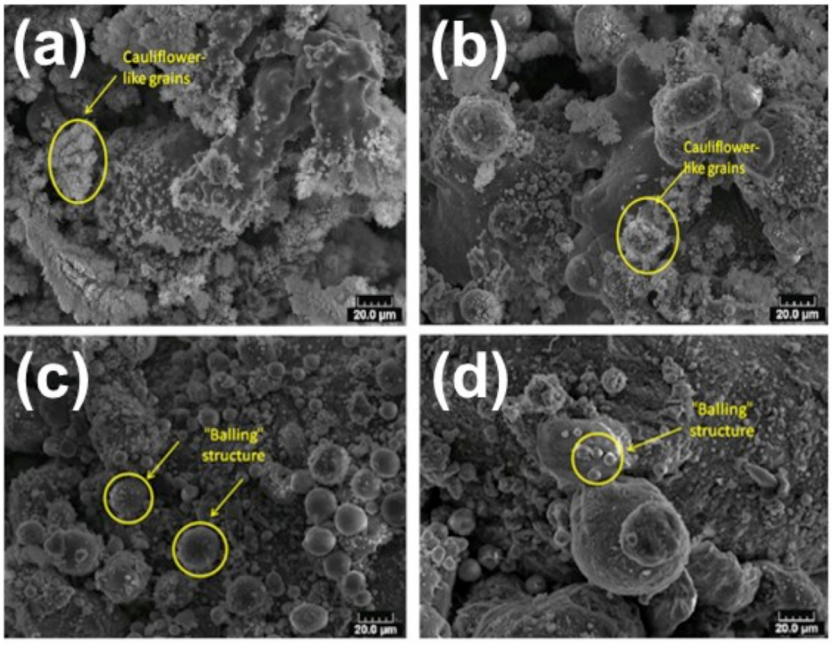

Fig. 6. SEM image of LAMed Mg–9%Al samples surface with variation of process parameters: (a) 10 W, 0.01 m/s; (b) 15 W, 0.02 m/s; (c) 20 W, 0.04 m/s; (d) 15 W, 0.04 m/s [55].

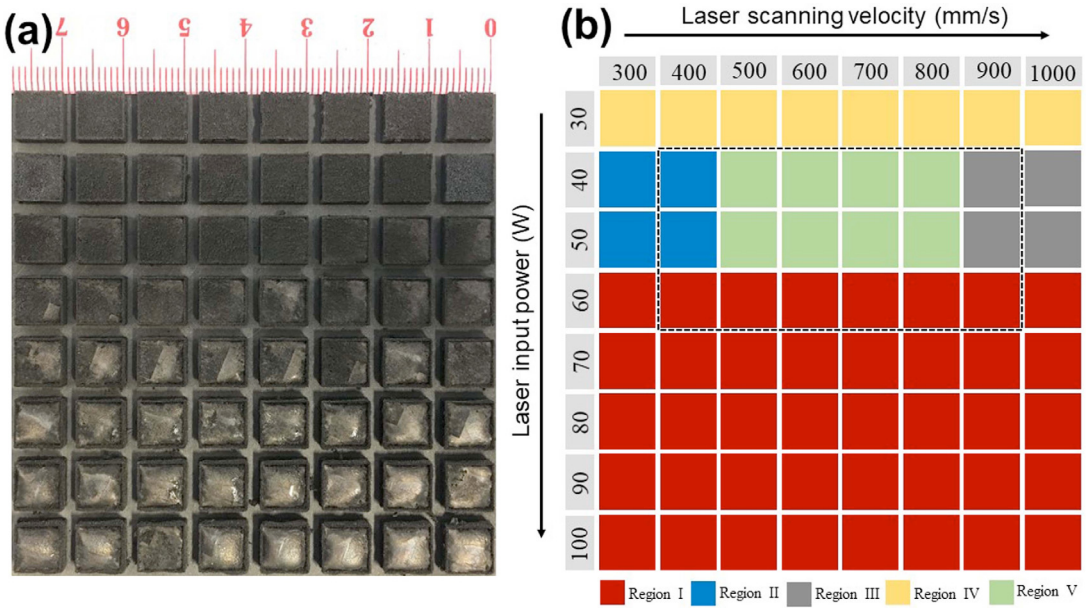

Fig. 7. Macro morphology of the LAMed ZK60 Mg-based alloys (a) and the corresponding laser processing parameters used (b) [56].

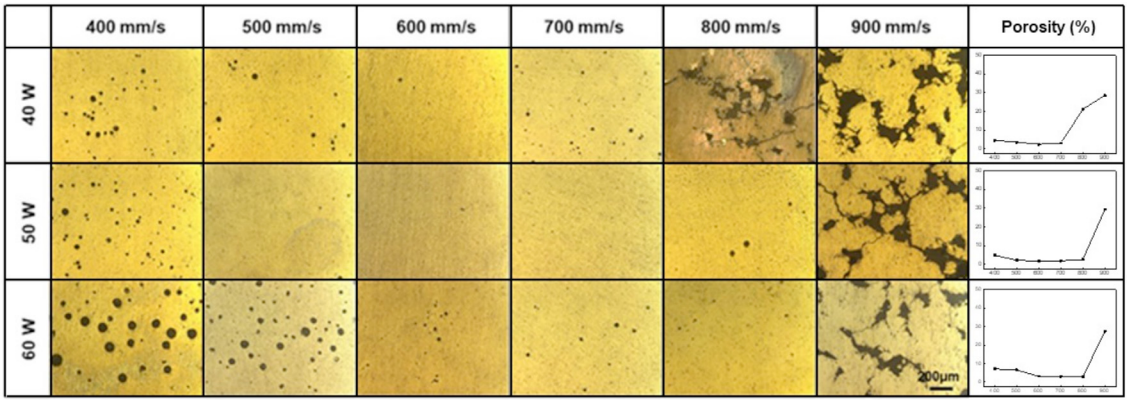

Fig. 8. OM image at low magnification and porosity for LAMed ZK60 Mg-based alloys at laser power of 40–60 W and scanning velocity of 400–900 mm/s as marked by black-dotted rectangle in Fig. 7(b) [56].

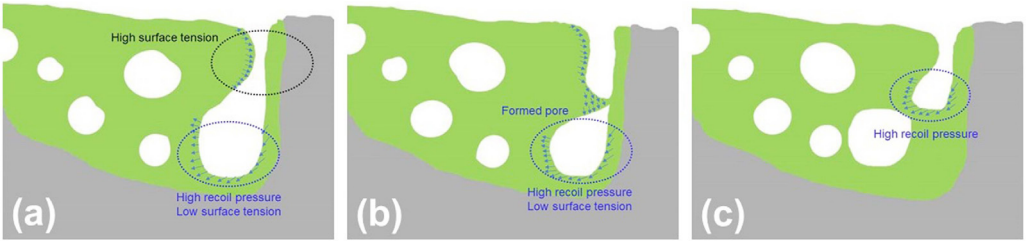

Fig. 9. Schematic diagram of keyhole mode porosity [56].

irradiated. As a consequence, recoil pressure is obviously increased, together with the decrease of surface tension. This would keep the keyhole open at this stage. With the increase of time, the surface tension is increased in the upper region of the keyholes, resulting in the closing of the cooling region in the upper region and the formation of pores (Fig. 9(b)). At the same time, the laser would continue to irradiate the depression region and form a strong downward flow below the depression region, leading to the pores further back into the melting pool (Fig. 9(c)).

Wei et al [48]. established a relationship (Fig. 10) between laser energy density E and the formability of AZ91D magnesium alloy. They divided the processing map into four zones based on formability. In zone A, due to the low boiling point and high vapor pressure of magnesium, powder evaporation exerted a high recoil pressure on the melting pool, and the

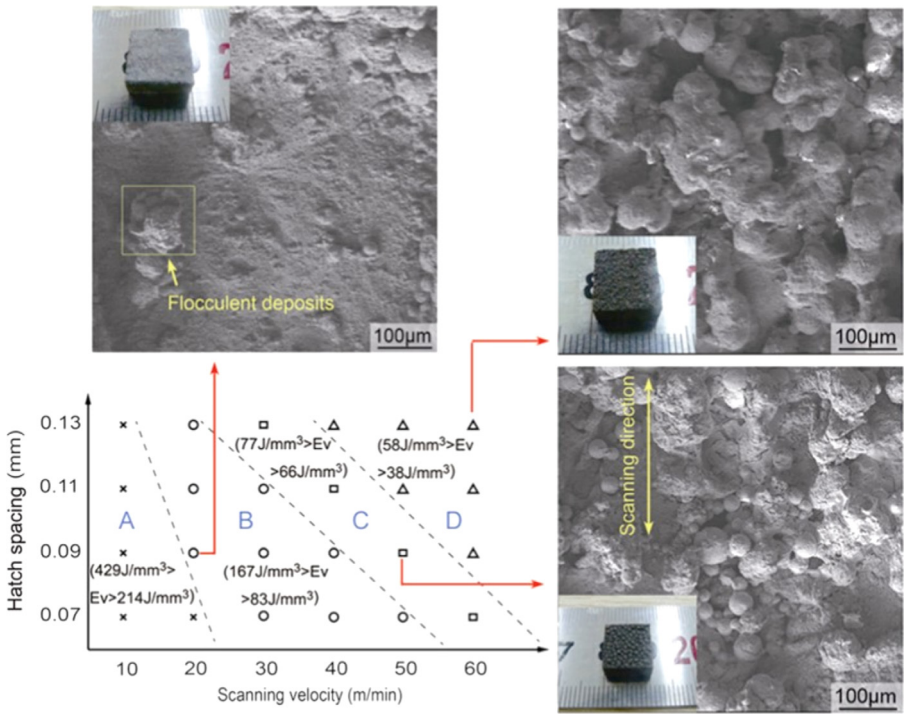

Fig. 10. Relationship between the laser energy density and the formability of AZ91D magnesium alloy [48].

melting pool together with the surrounding unmelted powders was blown away. LAM process failed when the laser energy density E was above 214 J/mm^3. In zone B, though macro-defects-free samples could be obtained at an energy density of 83 J/mm^3–167 J/mm^3, flocculent depositions and distorted scanning tracks were still observed on the samples prepared at 167 J/mm^3, which can be attributed to the evaporation of metal powders. In zone C, balling phenomenon appeared on the samples obtained at energy density of 66 J/mm^3 to 77 J/mm^3. In zone D, loose samples with poor mechanical strength were obtained owing to incomplete melting of powders. The sample with the highest relative density of 99.52% was obtained at an energy density of 167 J/mm^3.

The surface morphology and relative density of LAMed ZK60/ bioglass (BG) magnesium matrix composites prepared by different laser energy density are shown in Fig. 11 (Yang et al [60].). It is noticed that a few pores and unmelted powder particles were present between adjacent melted layers prepared at an energy density of 138.89 J/mm^3. In addition, the sample exhibited a low relative density of 86.7%. With the increase of energy density to 158.73 J/mm^3, the number of unmelted powder particles and pores was decreased and the sample with a higher density of 93.4% was obtained. When the energy density was increased to 185.19 J/mm^3, a smooth surface free of obvious holes were achieved, and the density of the sample increased to 97.6%. However, further increasing the energy density to 222.22 J/mm^3 resulted in a rough surface with balls, decreasing the density to 94.2%.

Yang et al [61]. investigated the effect of energy density on the formability of LAMed magnesium as shown in Fig. 12. This particular study revealed that some pores appeared on the sample fabricated by a low energy density of 6.0 J/mm, which can be attributed to the partially melted particles on the bottom of each layer. With the energy density was increased to 8.0 J/mm, the pores disappeared while a few partially melted particles were present. Pore-free sample prepared by an energy density of 10.0 J/mm was achieved due appropriate laser energy input. However, cracks appeared in the sample obtained at a higher energy density of 12.0 J/mm, which was attributed to the high residual thermal stress present. Zhu et al [62]. also reported that shrinkage behavior in direct laser sintering of metallic powder and the thermal shrinkage increased with the increase of laser energy input.

In conclusion, laser energy density plays an important role on the formability of LAMed samples. Several studies have reported the relative density of Mg-9Al, Mg-Zn, ZK60 and Mg-3.4Y-3.6Sm-2.6Zn-0.8Zr prepared by LAM [44,51,55,63], with the value ranging from 82% to 99.52%. These works revealed that there is a critical laser energy density by which samples with high relative density can be obtained.

3. Characteristics of LAMed Mg-based alloys for biomedical application

3.1. Chemical composition

Alloying is one of effective method to improve the mechanical properties and corrosion resistance of pure Mg. This is mainly attributed to the fact that the addition of alloying elements could alter the microstructural characteristics, especially the decrease of grain size in comparation with pure Mg. Among various Mg-based alloys, those containing Al or

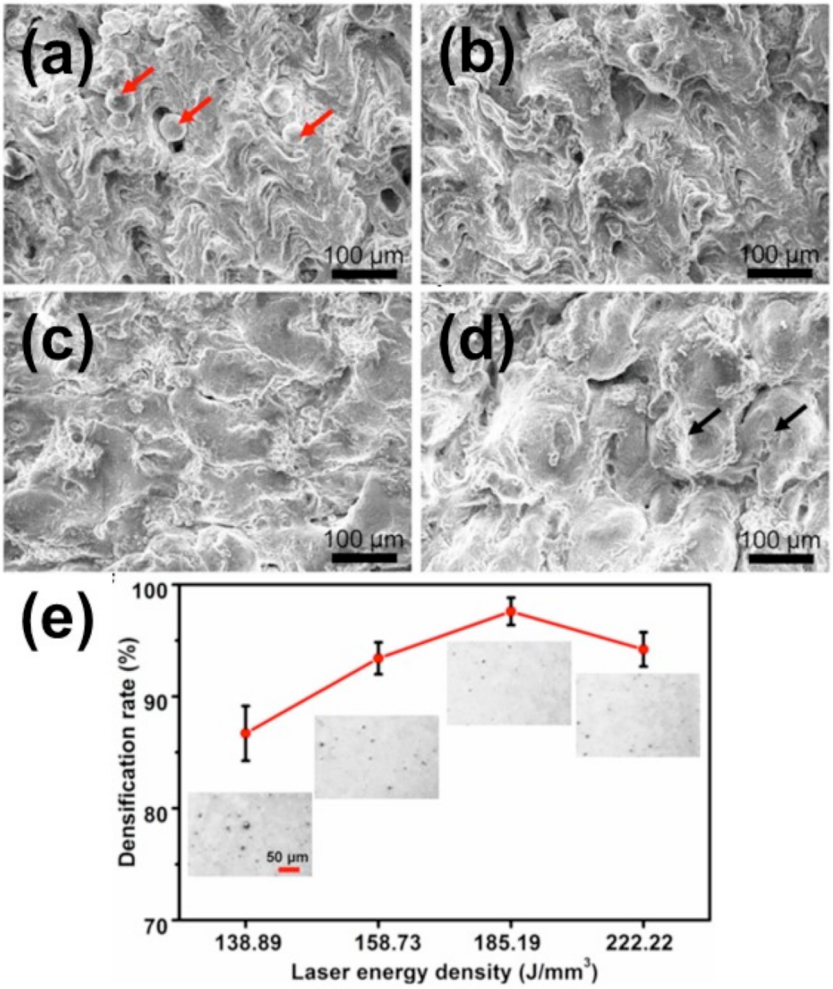

Fig. 11. Surface morphology and relative density of LAMed ZK60/BG Mg-based composite prepared by different laser energy density. (a) 138.89 J/mm^3, (b) 158.73 J/mm^3, (c) 185.19 J/mm^3, (d) 222.22 J/mm^3, (e) relatively density [60].

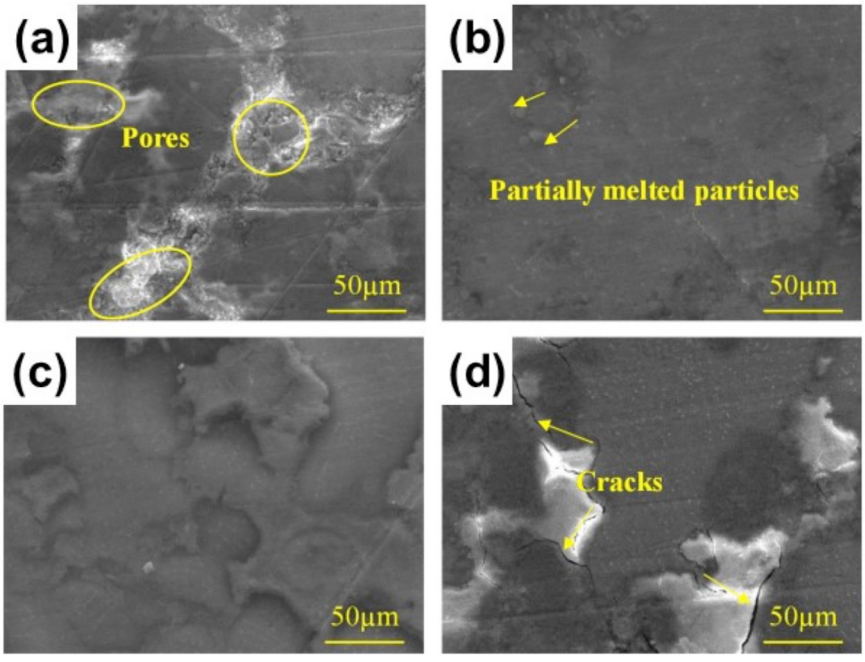

Fig. 12. Cross-section morphology of LAMed magnesium parts at various energy density. (a) 6.0 J/mm, (b) 8.0 J/mm, (c) 10.0 J/mm, (d) 12.0 J/mm [61].

RE have been widely reported due to the good combination of mechanical properties and corrosion resistance as well as mature fabrication technology [49,64–67]. Liu et al [65]. investigated the LAM of AZ61 Mg-based alloys and found that the corrosion resistance could be greatly improved when Ce was added. Liao et al [49]. prepared GW103K Mg-RE alloys by LAM, and showed that the as-fabricated sample exhibited much higher ultimate tensile strength and elongation compared with the alloy prepared by conventional sand cast process. Until now, most studies on Mg-based alloys focused on enhancing the properties for industrial purposes. As a consequence, current researches on Mg-based alloys for biomedical application originated from aerospace, defense and automotive fields. It should be, however, noticed that the addition of Al or RE elements, commonly used in industrial applications for improving the mechanical and corrosion resistance, in implants must be given careful consideration because of the latent toxic effects on human body. Al ion is known as a neurotoxicant likely to be a cause of Alzheimer's disease, and the release of Al ions can also weaken bone mineralization via inhibiting the formation of chemical bonds with implants [66]. In addition, RE elements are found to be residing in the degrading site of the implants [49]. Such incorporation may affect bone quality and health similar to other potentially toxic trace metals [68]. Therefore, there has been great interest in developing a new type of Mg-based alloys with a moderate corrosion rate, appropriate mechanical properties, good biocompatibility and bio-safety for medical applications. Recently, some researchers developed biologically safe Mg-based alloys with the addition of non-toxic elements such as Zn, Mn, Zr, Ca and Li and so on [33,34,51,69–71].

Zn is recognized as one of the essential elements in the human body and it takes part in almost all the physiological functions, indicating an excellent safety for biomedical applications [35]. Additionally, Zn is also an effective alloying element in strengthening and helps to eliminate the undesirable galvanic effect of impurities such as Fe and Ni. The addition of Zn contributes to the improvement in mechanical properties and corrosion resistance [35]. Mn plays an important role in improving the corrosion resistance through removing Fe and other heavy metal elements [27,70]. It exhibits no toxic effect at low concentration and is actively involved in the activation of multiple enzyme systems such as hydrolases, kinases, transferases, decarboxylases and mitochondrial respiration [27,70]. By adjusting the elemental content and type, researchers have designed binary, ternary or multi-elements Mg-based alloys, aiming at improving the corrosion resistance and mechanical properties for biomedical applications.

Liu et al [50]. fabricated porous Mg-Ca alloys by LAM and studied the effect of processing parameters on porosity and mechanical properties. It is found that the porosity decreased, and the compression performance increased with the laser energy density. In addition, it has been reported that mechanical properties and biocorrosion properties of Mg-Ca alloys can be significantly improved by adjusting the Ca content [72]. Moreover, Mg-Ca alloys exhibit no toxicity to cells and can contribute to the growth of bone according to cytocompatibility evaluation [72]. Wei et al [51]. explored the effects of Zn content on densification behavior, microstructure, and mechanical properties of Mg-Zn binary alloys prepared by LAM. Other researches [73] also revealed that Zn-containing Mg-based alloys displayed a lower *in vivo* degradation rate in comparation with pure Mg. Moreover, Cu-containing antibacterial Mg-based alloys were also developed recently, aiming at improving the antibacterial ability and cytocompatibility *in vivo*.

3.2. LAM of Mg matrix composites

Recently research regarding LAM of Mg matrix composites by incorporating bioactive ceramics such as BG has drawn much attention. It is noticed that these bioactive ceramics not only control the corrosion behavior of LAMed Mg matrix composites, but also possess a similar chemical composition and structure to the human bone. Meanwhile, these bioactive ceramics can act as nuclei for the formation of apatite and induce bone growth. Yang et al [16,60,74]. performed LAM technology to prepare Mg matrix composites by incorporating bioglass for bone repair. They revealed that the addition of bioglass could effectively increase the corrosion resistance, contribute to the growth and differentiation of cells, and improve apatite deposition. Yin et al [75]. also revealed that the incorporation of bioactive glass into Mg alloys by LAM resulted in improved corrosion resistance, bioactivity and cytocompatibility. The above research works indicate that Mg matrix composites prepared by LAM exhibit a great potential for biomedical applications. The properties of LAMed Mg matrix composites are reviewed in subsequent sections.

3.3. Microstructure of LAMed mg-based alloys

The properties of LAMed Mg-based alloys mainly depend on the microstructure and constituent phase such as grain size, grain boundary and phase distribution. The refined grains exert an important role on mechanical properties as well as the corrosion resistance of LAMed Mg-based alloys because it alters the grain boundary density and distribution. LAM is a rapid melting/solidification process with solidification rate of approximately 10^5 K s^{-1}, which can induce the formation of refined grains, non-equilibrium phases and homogeneity in microstructures [28–32]. According to the solidification theory, there are three microstructural morphologies (columnar, cellular, and equiaxed microstructure) depending on the parameters of G (temperature gradient in the melt ahead of the solidifying front) and v (rate of solidification), with G/v affecting the solid-liquid interface shape and $G \times v$ affecting the undercooling [76]. On the one hand, as the temperature gradient G is much larger in the top surface layer than that inside the layer, the ratio G/v is much larger in the top surface, which can contribute to the transition from columnar to equiaxed grain microstructure due to the faster nucleation rate in the top surface layer. On the other hand, a high value of $G \times v$ would result in a refined microstructure. Zumdick

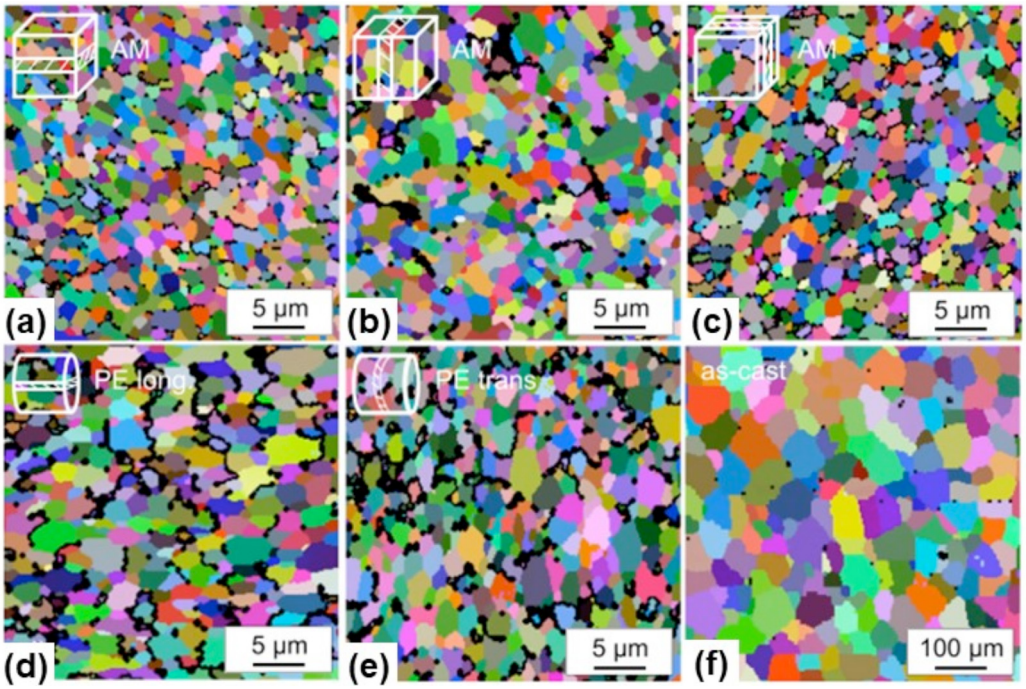

Fig. 13. Electron backscatter diffraction of WE43 prepared by different technique. (a)-(c) LAMed sample in different section, (d) and (e) extruded sample in different section, (f) cast sample [52].

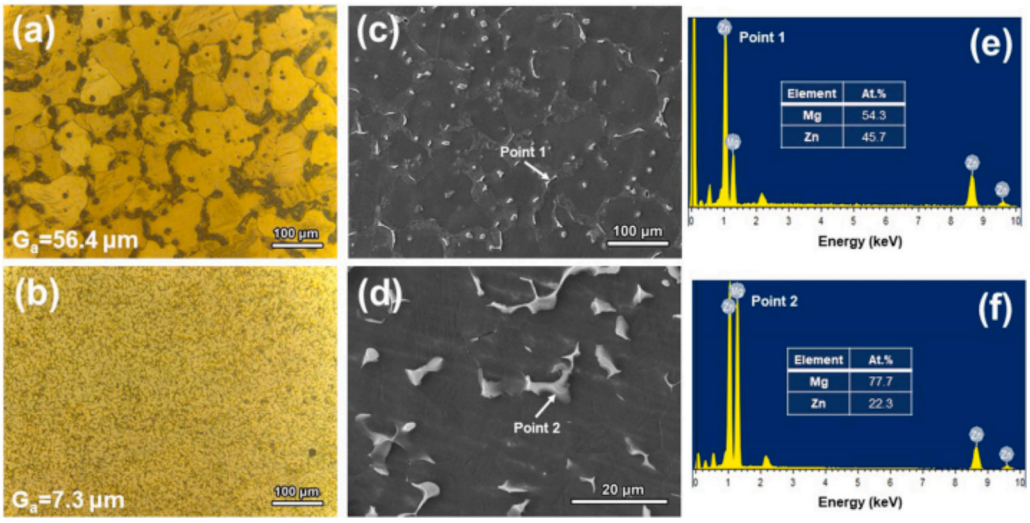

Fig. 14. Microstructure of cast ZK60 (a), (c); LAMed ZK60 (b), (d) and EDS results corresponding to point 1 (e) and point 2 (f) [56].

et al [52]. carried out a comparative study on the microstructure of WE43 Mg alloys prepared by LAM, powder extrusion and casting as shown in Fig. 13. This particular research clarified that the LAMed sample possessed a grain size of 1.0 to 1.1 μm, in comparison with a slightly larger grain size of 1.3 μm for extruded samples and much larger grain size of 44.3 μm for cast samples, indicating that the rapid solidification, an inherent characteristics of LAM, can effectively refine grains.

Figure 14 shows the microstructure and EDS results of the precipitated phases for cast ZK60 and LAMed ZK60 reported by our group [56]. It is noticed that the average grain size for cast ZK60 and LAMed ZK60 was 56.4 μm and 7.3 μm, respectively. The average grain size of LAMed ZK60 was much smaller than that of cast ZK60, which can be attributed to the rapid cooling characteristics of LAM. Both cast and LAMed ZK60 samples exhibited an α-Mg matrix with precipitated phases, and these precipitated phases contained 54.3 at% Mg and 45.7 at% Zn in cast ZK60, and 77.7 at% Mg and 22.3 at% Zn in LAMed ZK60, indicating that the precipitated phases were mainly MgZn for cast ZK60 and Mg_7Zn_3 for LAMed ZK60, respectively. The different precipitated phases formed in cast ZK60 and LAMed ZK60 were due to the high cooling rate of LAM, in which the decomposed reaction

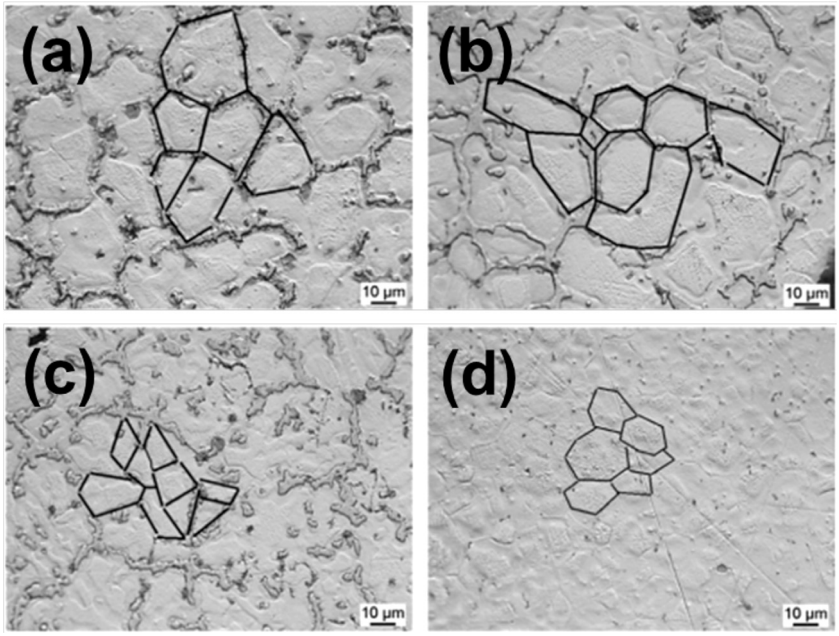

Fig. 15. OM image showing the characteristic microstructures as a function of energy density: (a) 20 J/mm^2; (b) 15 J/mm^2; (c) 10 J/mm^2; (d) 7 J/mm^2 [55].

($Mg_7Zn_3 \rightarrow \alpha$-Mg + MgZn) was inhibited, leading to the presence of Mg_7Zn_3 in LAMed ZK60.

Zhang et al [55]. prepared Mg-9%Al alloys by LAM through varying the laser processing parameters. It shows that the alloys exhibited equiaxed grains with the average size of 10–20 μm and the grains were refined with the decrease of laser energy density (Fig. 15). The constituent phases consisted mainly of α-Mg, $Mg_{17}Al_{12}$, MgO and Al_2O_3. MgO and Al_2O_3 were formed by the oxidation reaction of remaining Al with a little oxygen in the working atmosphere during LAM.

Wei et al [51]. investigated the Zn content on the microstructural evolution of LAMed Mg-xZn (x = 1, 2, 4, 6, 8, 10 and 12) alloys. The addition of Zn exerted a significant effect on the microstructure. The LAMed Mg-xZn alloys mainly exhibited α-Mg matrix with hexagonal close-packed structure and Mg_7Zn_3 eutectic phase with orthorhombic structure. It is worth mentioning that no oxide inclusions including MgO and ZnO were present, which could be attributed to the strict control of the content of O_2 and H_2O during the LAM process. According to the binary phase diagram of Mg-Zn [77], a mixture of α-Mg and Mg_7Zn_3 would be formed through the eutectic reaction of the Mg-Zn alloy at 340 °C, and then α-Mg and MgZn would appear via eutectoid reaction of the Mg_7Zn_3 eutectic phase at 325 °C. However, owing to the rapid melting/cooling rate during the LAM process, this eutectoid reaction, *i.e.* $Mg_7Zn_3 \rightarrow \alpha$-Mg + MgZn, would be inhibited. As a consequence, Mg_7Zn_3 was observed in the LAMed samples instead of MgZn. Manne et al [78]. also reported similar observation in the Mg-Zn alloys prepared by LAM. The addition of Zn obviously alters the morphology and content of the Mg_7Zn_3 eutectic phase as shown in Fig. 16. As the Zn content increased, the morphology exhibited a gradual transition from granular shape to nearly reticular structure (Fig. 16(a)–(g)) and the fraction of Mg_7Zn_3 eutectic phase also increased continuously with the peak value of 18.68% when x = 12 (Fig. 16(h)).

Due to the antibacterial ability of Cu ion, Cu-containing ZK60 alloys was developed and prepared by LAM [47]. The average grain size of ZK60-xCu (x = 0, 0.2, 0.4, 0.6 and 0.8) alloys decreased gradually with the increase of Cu, with the value of 13.6, 8.8, 6.2, 5.1 and 4.5 μm. The decrease in grain size could be attributed to the fact that Cu atoms were present in the diffusion layer in the front of the solid-liquid interface during the solidification, leading to the constitutional undercooling and thus inhibiting the growth of grain. A comparative study of the microstructural difference between the LAMed ZK60 and cast ZK60 was reported in reference [56]. The average grain size of LAMed ZK60 was much smaller than that of cast ZK60, being 56.4 μm for cast ZK60 and 7.3 μm for LAMed ZK60. The decrease in the grain size for the LAMed ZK60 was mainly due to the high cooling rate, an inherent characteristic of LAM.

Yang et al [60] investigated the microstructure of LAMed ZK60/BG parts at various energy density as shown in Fig. 17. It is noticed that the BG particles were irregular-shaped, mainly composed of Si and exhibited a more uniform distribution with increase of energy density. The distribution state of BG particles was dependent on the laser energy density. This phenomenon can be attributed to the fact that the BG particles could not be rearranged effectively in the melting pool at low energy density due to weak Marangoni convection, resulting in inhomogeneous distribution. With the increase of energy density, the intensified Marangoni convection and the high temperature would contribute to a homogeneous distribution of the BG particles.

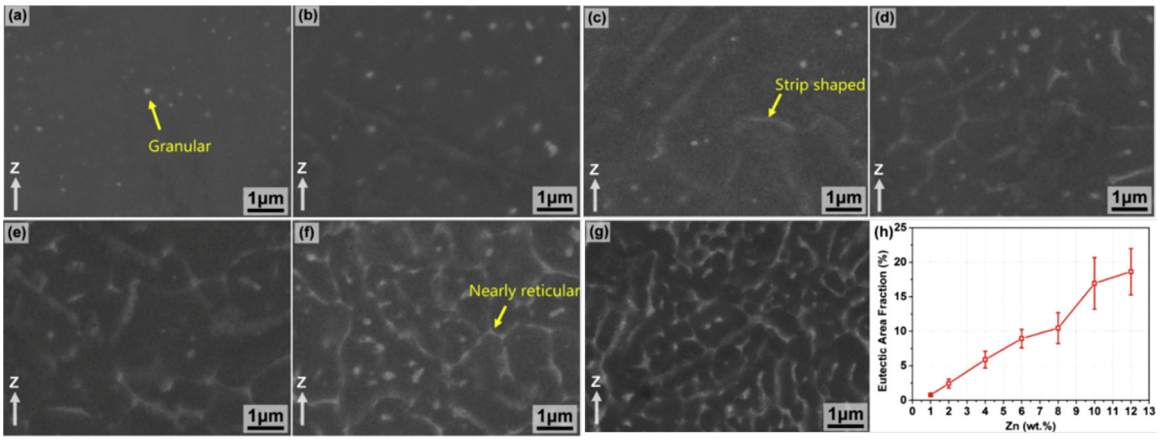

Fig. 16. SEM image of the LAMed Mg-*x*Zn: (a) $x = 1$, (b) $x = 2$, (c) $x = 4$, (d) $x = 6$, (e) $x = 8$, (f) $x = 10$, (g) $x = 12$, (h) area fraction of eutectic phase [51].

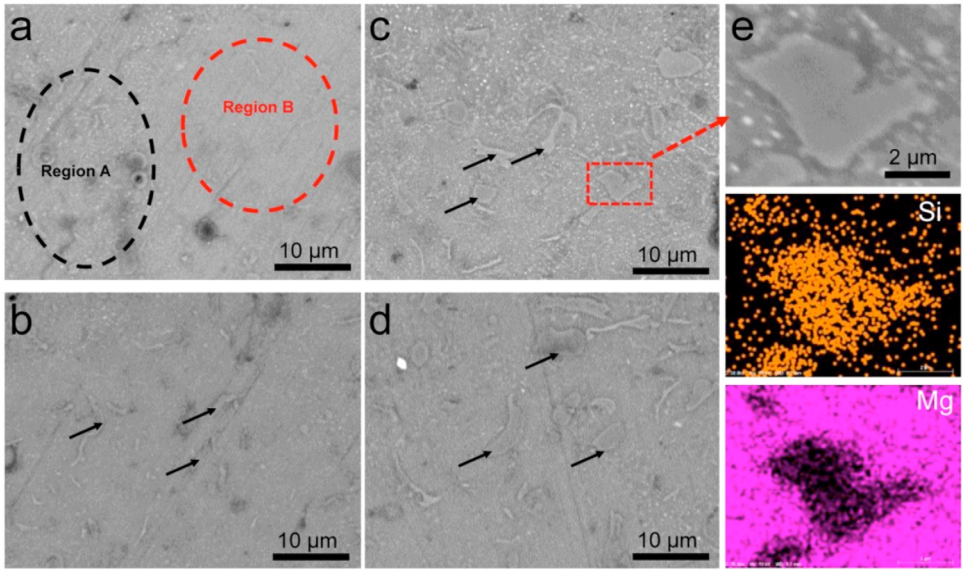

Fig. 17. SEM image of LAMed ZK60/BG parts at various energy density. (a) 138.89 J/mm^3, (b) 158.73 J/mm^3, (c) 185.19 J/mm^3 and (d) 222.22 J/mm^3. (e) The elemental maps corresponding to the marked area in Fig. 17 (c) [60].

In addition, Yang et al [74]. also investigated the effect of different BG on the microstructure of LAMed ZK60 as shown in Fig. 18. They reported that in general there was no obvious negative effect of the incorporated BG particles on the densification behavior. The ZK60/BG and ZK60/mesoporous BG samples exhibited finer equiaxed grains compared to the ZK60. The Ca-, Si- and O-rich BG particles were uniformly distributed in Mg matrix, which is different from other reports that the agglomeration of BG particles easily occurred in Mg matrix composites prepared by other techniques. The uniform distribution of BG particles can be attributed to the fact that Marangoni convection could effectively promote the uniform distribution of the particles.

3.4. Mechanical properties of LAMed Mg-based alloys

Implants are required to provide stable and appropriate mechanical support during the healing period. The hardness and elastic modulus of pure Mg, cast ZK60, LAMed ZK60, natural bone and conventional metallic implant materials are shown in Fig. 19. The hardness and elastic modulus of pure Mg, caste ZK60 and LAMed ZK60 are much closer to those of natural bone than conventional metallic implant materials such as Ti-based alloys, stainless steel and Co-Cr alloys. Therefore, the "stress shielding" effects can be significantly reduced by the use of Mg-based alloys implants.

According to previous reports, there are three main routes to improve the mechanical properties of LAMed Mg-based alloys, including alloying, varied laser processing parameters and post heat treatment. On the one hand, researchers have tried to improve the mechanical properties through adding various alloying elements such as Zn, Zr, Al, Ca and RE, etc. Liu et al [50]. prepared porous Mg-Ca alloys by LAM, aiming at improving the mechanical properties. The average microhardness of LAMed Mg-Ca alloys was approximately

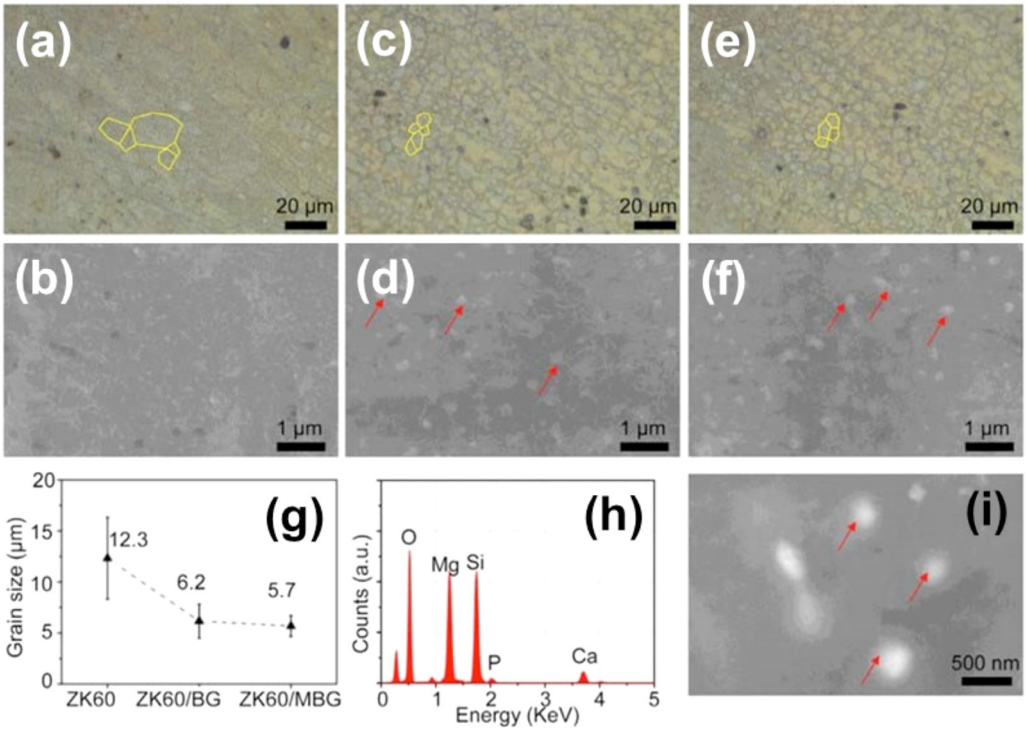

Fig. 18. SEM image of LAMed ZK60 (a) and (b), ZK60/BG (c) and (d), ZK60/mesoporous BG (e) and (f); grain size (g); Typical EDS result of the marked area (h); High resolution SEM image of ZK60/mesoporous BG [74].

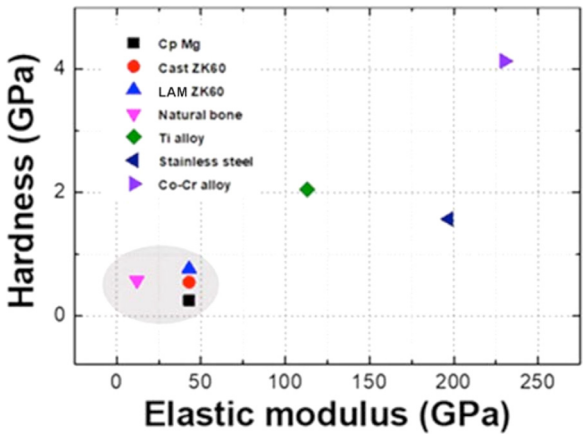

Fig. 19. Comparison of hardness and elastic modulus of pure Mg, cast ZK60 and LAMed ZK60 with natural bone and conventionally metallic implant materials [56].

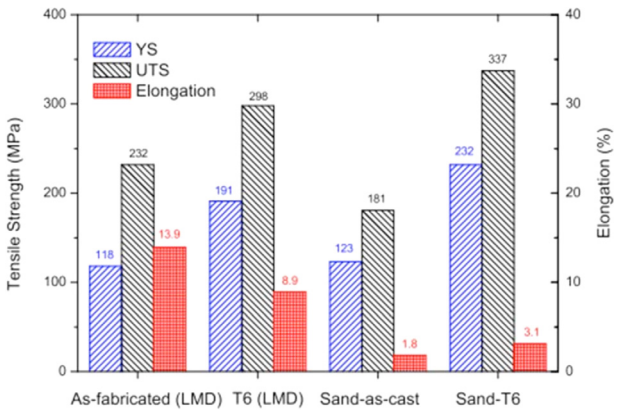

Fig. 20. Ambient temperature tensile properties of LAMed and sand cast GW103K alloys before and after T6 treatment [49].

65 HV and much higher than that of the cast pure Mg (35.36 HV) and LAMed pure Mg (52 HV). However, there are reports showing that the addition of Zn in LAMed Mg-1Zn alloy would decrease the mechanical properties due to the increase of defects inside the samples [51], leading to fluctuation of mechanical properties, and hence poor service reliability. On the other hand, in Mg-based samples prepared by LAM under optimized parameters (Wei et al [44].), a comparative microhardness with the wrought Mg-Zn-Zr alloys was made. In addition, heat treatments such as solution and aging treatments are also adopted to adjust the mechanical properties in biomedical applications. Solution treatment decreases strength, but increases ductility. Aging treatments might result in the opposite effect. Liao et al [49]. performed tensile tests of LAMed GW103K Mg-RE alloys before and after heat treatment as shown in Fig. 20. Yield strength (YS), ultimate tensile strength (UTS) and elongation of the LAMed and T6-treated LAMed GW103K alloys are 118–232 MPa–13.9% and 191–298 MPa–8.9% at ambient temperature, respectively. Moreover, the LAMed samples exhibited comparable YS (−5 MPa), much higher UTS (+51 MPa) and elongation (+12.1%) in comparation with sand cast alloy. The YS and UTS of the T6-treated LAMed sample were about

Table 2
Mechanical properties of Mg-based sample prepared by LAM and traditional fabrication methods.

Sample	Yield strength (MPa)	Tensile strength (MPa)	Elongation (%)
LAMed AZ91D [48]	237–254	274–296	1.83–3
LAMed GW103K [49]	118	232	13.9
LAMed GW103K-T6 [49]	191	298	8.9
LAMed Mg-1Zn [51]		148	11
LAMed WE43 [52]	296.3	308.0	11.9
Extruded WE43 [52]	284.4	306.6	14.3
Extruded AZ91D [79]		295	13
As-cast AZ91D [79]	145	248	7.4
Die-cast AZ91D [48]	160	230	3
As-cast GW103K [49]	123	181	1.8
As-cast Mg-1Zn [51]		102	7
As-cast WE43 [52]	145.4	189.2	4.4

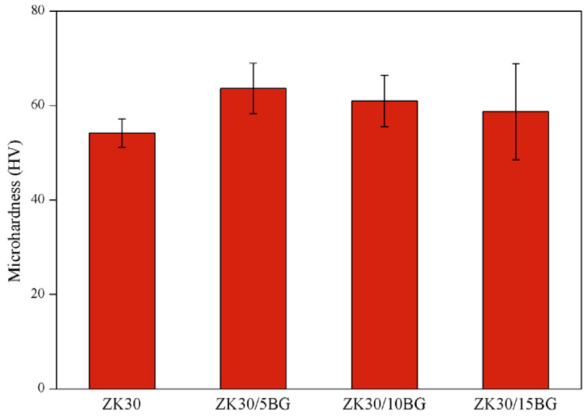

Fig. 21. Microhardness of LAMed ZK30/xBG as a function of BG content [75].

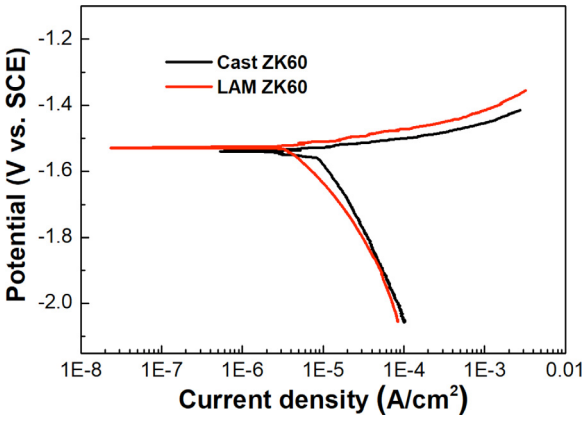

Fig. 22. Potentiodynamic polarization curve obtained in Hanks' solution at 37°C for cast ZK60 and LAMed ZK60 [56].

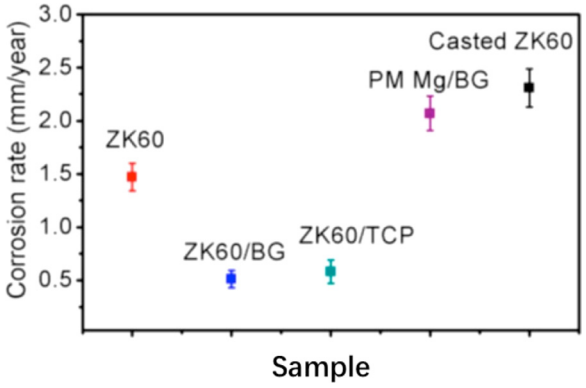

Fig. 23. The corrosion rate of Mg-based alloys in simulated body fluid. BG: Bioglass, TCP: Calcium phosphate tribasic, PM: Powder metallurgy process [60].

40 MPa lower than those of sand cast alloy, with relatively higher elongation (+5.8%), and the decrease of YS and UTS can be attributed to the evaporation loss of Gd and Y elements during LAM process, grain growth and formation of GdH_2 particles during T6 heat treatment.

In addition, some researchers developed LAM of Mg matrix composites and investigated the effect of BG content on the microhardness. Yin et al [75]. reported that the addition of BG particle can effectively increase the hardness of ZK30 prepared by LAM (Fig. 21). However, the hardness was not monotonically increased with the addition of more BG particles. This phenomenon was attributed to the change in microstructure. Yang et al [60]. also clarified that the LAMed ZK60/BG, with uniformly distributed BG particles in the matrix, could significantlu enhance the strength due to the second-phase strengthening effect.

The mechanical properties of Mg-based samples with the same chemical composition fabricated by different methods are summarized in Table 2. In general, the LAMed samples exhibited comparable or even superior strength and elongation compared to the samples with the same chemical composition fabricated by traditional methods. This phenomenon can be attributed to grain boundary strengthening effect. The strength is inversely proportional to the square root of the grain size according to the Hall-Petch relationship. In addition, the rapid solidification led to an extension of the solubility limit, and enhanced solution strengthening of LAMed samples.

3.5. Corrosion properties of LAM Mg-based alloys

The high corrosion rate of Mg-based implants *in vivo* is the biggest hurdle to overcome as it will lead to a premature dis-

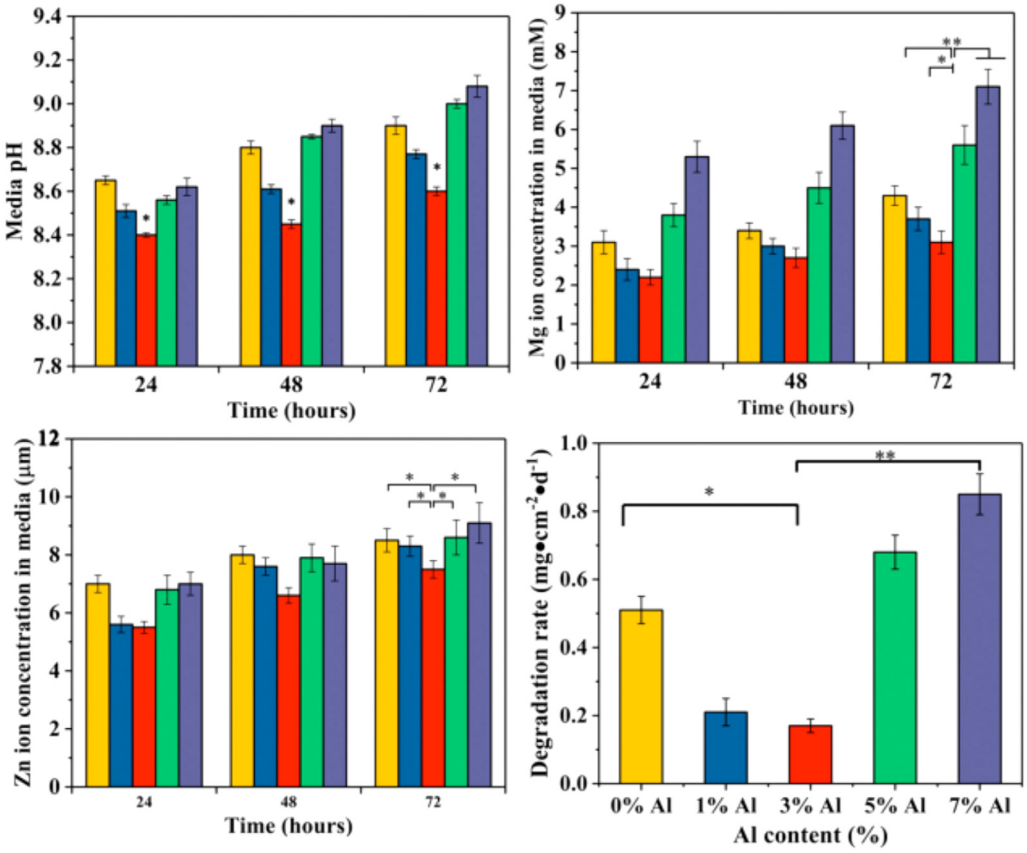

Fig. 24. The biodegradable behavior of Mg-*x*Al-Zn prepared by LAM (a) pH, (b) Mg^{2+} ion concentration, (c) Zn^{2+} ion concentration and (d) degradation rate calculated through Mg^{2+} ion concentration [53].

integration, loss of mechanical integrity, and local hydrogen accumulation. The corrosion of Mg-based alloys in aqueous medium is an electrochemical process and can be expressed according to [36]:

$$\text{Anodic reaction: } Mg \rightarrow Mg^{2+} + 2e^- \quad (4)$$

$$\text{Cathodic reaction: } 2H_2O + 2e^- \rightarrow H_2(g) + 2OH^- \quad (5)$$

$$\text{Overall: } Mg + 2H_2O \rightarrow H_2 + Mg(OH)_2 \quad (6)$$

It is noticed that the degradation of Mg-based alloys resulted in the release of OH^-, leading to an increase of pH value progressively during immersion. However, $Mg(OH)_2$ is unstable and offers very low corrosion resistance, especially in chloride-containing environments (simulated body fluid). The degradation of $Mg(OH)_2$ can be expressed as following:

$$Mg(OH)_2 + 2Cl^- \rightarrow MgCl_2 \quad (7)$$

$$Mg + 2H_2O \rightarrow Mg(OH)_2 + H_2\uparrow \quad (8)$$

$$Mg + 2Cl^- \rightarrow MgCl_2 \quad (9)$$

It has been reported that the formation of $MgCl_2$ would deteriorate the corrosion resistance in that $MgCl_2$ was moderately soluble [80]. Therefore, fresh Mg surface was exposed to the solution and the above reaction (4–9) occur repeatedly until the Mg-based alloys were completely degraded. Nevertheless, the formed $Mg(OH)_2$ can delay the contact between the Mg-based alloys and solution to some extent [81]. In general, the high corrosion rate or degradation rate of the Mg-based alloys is still one of the main reasons that restrict their wide applications as medical biomaterials. Moreover, an adverse biological reaction would occur resulting from local alkalization and formation of hydrogen bubbles in the physiological environments [22]. Previous researches have clarified that a lower degradation rate could be achieved for the Mg alloys with small grain size and homogeneous microstructure, mainly resulting from improved passivation and decreased micro-galvanic attack [36,80]. The corrosion resistance of Mg–Y–RE magnesium alloys with grain size from 0.7 μm to 70 μm was investigated by Argade et al [36]., and they reported a one-order magnitude increase in corrosion resistance could be achieved for samples with small grain size. Alvarez-Lopez et al [82]. investigated the degradable behavior of AZ31 magnesium alloy with different grain sizes in phosphate-buffer solution. It was found that AZ31 alloy with the finest grain size exhibited the highest corrosion resistance as indicated by the highest charge transfer resistance. The increase in corrosion resistance of hot-rolled AZ31 alloy [26], hot extruded Mg–Ca alloy [2] and ZK60 alloy [34] were also achieved due to grain refinement induced dur-

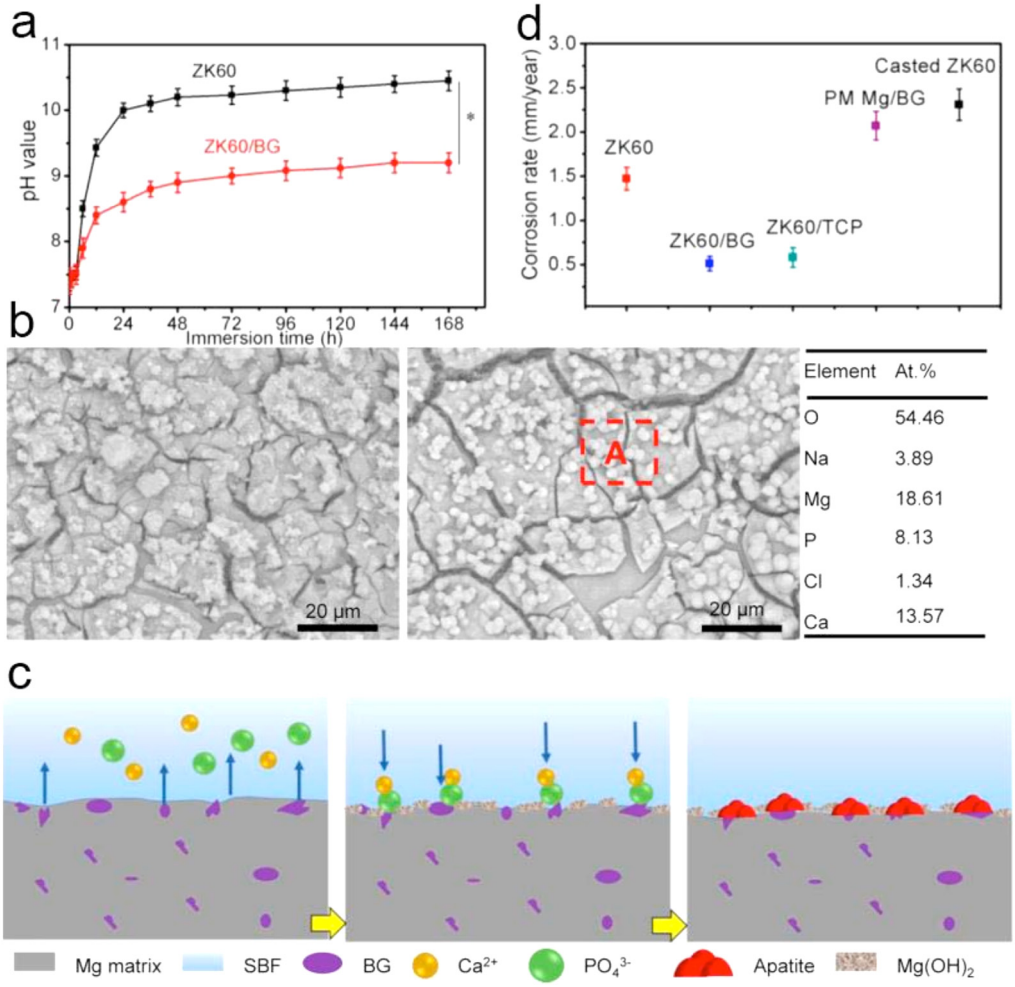

Fig. 25. Corrosion properties of LAMed ZK60/xBG. (a) pH value variation as a function of time, (b) corroded surface, (c) corrosion mechanism during immersion, (d) degradation rate of Mg-based alloy [60].

ing the forming processes. Therefore, LAMed is recognized as an effective way to enhance the corrosion resistance of Mg-based alloys for biomedical application because LAM has the advantage of homogenizing and refining the microstructure, and inhibiting the formation of the secondary phases. Until now, the studies on corrosion behaviors of LAMed Mg-based alloys are scarcely reported and most studies mainly focused on the formability quality and mechanical properties of LAMed samples. Potentiodynamic polarization curve obtained in Hanks'solution at 37 °C for cast ZK60 and LAMed ZK60 are shown in Fig. 22 as reported by our group [56]. The LAMed ZK60 possessed a lower corrosion current density of 8.89 μA/cm^2 with a nobler corrosion potential of -1.52 V *vs.* SCE. Moreover, both the cathodic and anodic current density of LAMed ZK60 were lower than that of cast ZK60 at the same potential, implying a lower hydrogen evolution rate and Mg matrix dissolution rate. The corrosion rate of Mg-based alloys in simulated body fluid is summarized as shown in Fig. 23. The LAMed ZK60 samples with refined grain and uniform microstructure possessed lower corrosion rate as compared to cast ZK60.

Mg-based alloys prepared by LAM exhibited an improved corrosion resistance in comparation with the samples prepared by casting or powder metallurgy. In addition, Shuai et al [53]. investigated the effect of grain size and the secondary phases on the biodegradable behaviors of Mg-*x*Al-Zn prepared by LAM (Fig. 24), and reported that the corrosion resistance increased firstly and then decreased with the addition of Al using electrochemical test, pH tests and ion concentration measurement. This can be attributed to the balanced effect between grain size and the secondary phases as grain refinement can slow down degradation, while the increase of intermetallic phase in Mg-*x*Al-Zn would deteriorate it.

Yang et al [60]. performed immersed tests to study the degradation property of LAMed ZK60/BG and ZK60 with results shown in Fig. 25, and they reported that the addition of BG particles could promote the deposition of apatite and the deposited apatite exhibited a stable and compact structure, which could protect the sample surface from corrosion. Moreover, the comparison of corrosion rate among various Mg-based alloys prepared by different techniques indicates

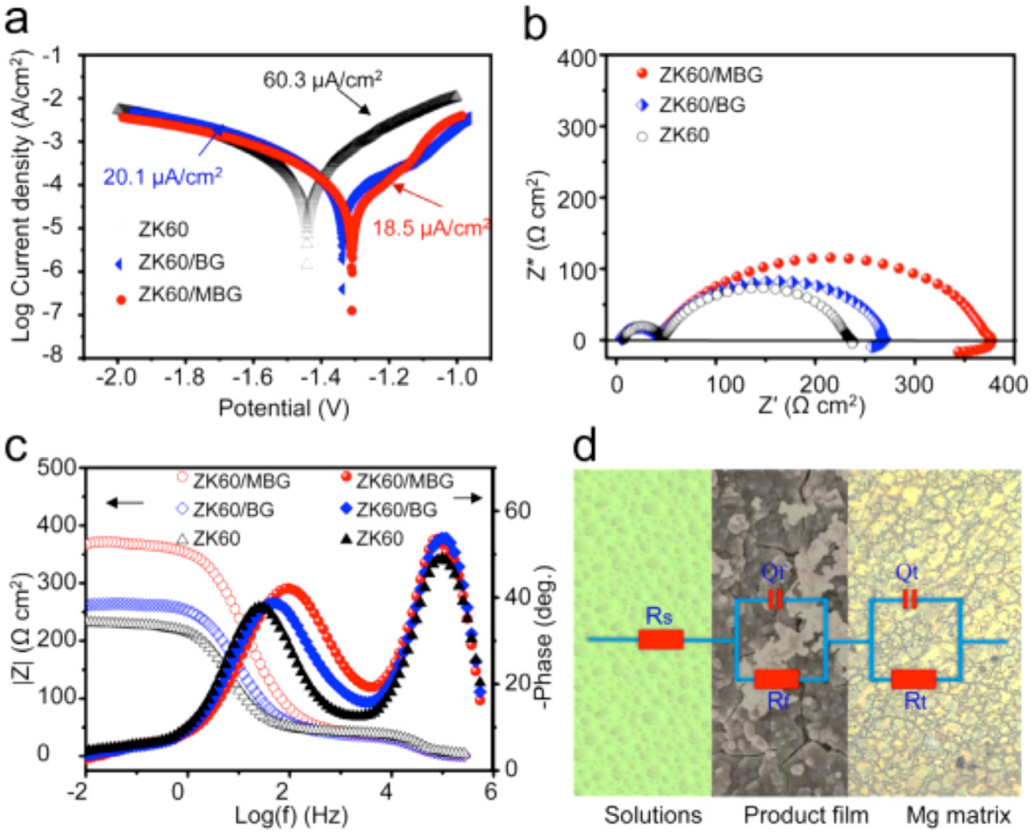

Fig. 26. Corrosion behavior of LAMed ZK60, ZK60/BG, ZK60/mesoporous BG. (a) Tafel polarization curves, (b) EIS plots, (c) Bode plots and (d) equivalent electrical circuit [74].

Table 3
Corrosion properties in simulated body fluid of Mg-based sample prepared by LAM and traditional fabrication methods.

Sample	Corrosion current density (μA/cm^2)	Corrosion potential (V)	Corrosion rate (mm/y)
LAMed ZK30 [46]	17.8	-1.52	0.41
LAMed ZK30-0.1 wt%Cu [46]	28.2	-1.51	0.64
LAMed ZK30-0.2 wt%Cu [46]	38	-1.48	0.87
LAMed ZK30-0.3 wt%Cu [46]	47.8	-1.46	1.09
LAMed ZK60 [56]	8.89	-1.52	0.2
LAMed ZK60-5wt%BG [60]	16.6	-1.31	0.38
LAMed AZ61 [54]	39.6	-1.46	0.9
LAMed AZ61-3wt%CaO [54]	30.2	-1.43	0.69
LAMed AZ61-6wt%CaO [54]	22.3	–1.4	0.51
LAMed AZ61-9wt%CaO [54]	10.2	-1.37	0.23
LAMed AZ61-12wt%CaO [54]	27.3	-1.38	0.62
As-cast ZK60 [56]	18.5	-1.55	0.42
As-cast Mg–4.0Zn–0.2Ca [24]	267	-1.7	2.13
As-extruded Mg–4.0Zn–0.2Ca [24]	243	-1.677	1.98
As-cast Mg-2Zn-0.6Zr [83]	20.27	-1.509	0.46
As-cast Mg-2Zn-0.6Zr-0.2Nd [83]	16.21	-1.494	0.37
As-cast Mg-2Zn-0.6Zr-0.6Nd [83]	28.99	-1.531	0.66
As-cast Mg-2Zn-0.6Zr-1Nd [83]	42.78	-1.56	0.98
As-drawn AZ31 [84]	17.73	-1.48	0.4
As-cast ZK40 [84]	37.19	-1.49	0.84
As-cast ZK40-T6 [84]	38.07	-1.55	0.86

that the LAMed ZK60/BG showed the lowest corrosion rate. Yang et al [74]. carried out a comparative study of corrosion resistance between the LAMed ZK60 and Mg matrix composites as shown in Fig. 26. This particular study revealed that LAMed ZK60 matrix composites exhibited more positive corrosion potentials, smaller corrosion current densities and larger impedance loops compared to the LAMed ZK60. The above research demonstrated that the incorporated BG particles could significantly enhance the corrosion resistance of Mg matrix.

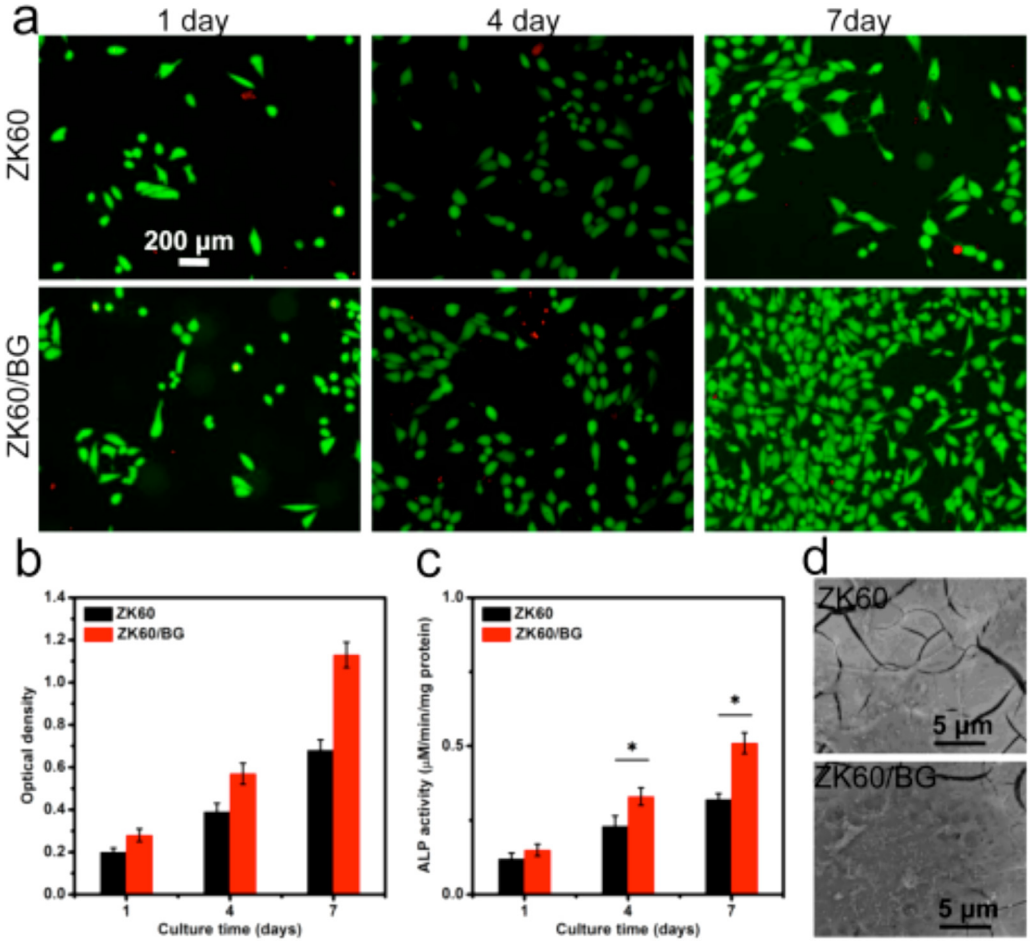

Fig. 27. Biocompatibility of LAMed ZK60 and ZK60/BG. (a) Live/dead staining images, (b) CCK-8 results and (c) ALP activities of MG-63 cells cultured in the extracts for 1, 4 and 7 days; (d) SEM showing the cells' direct culture on ZK60 and ZK60/BG after 3 days [60].

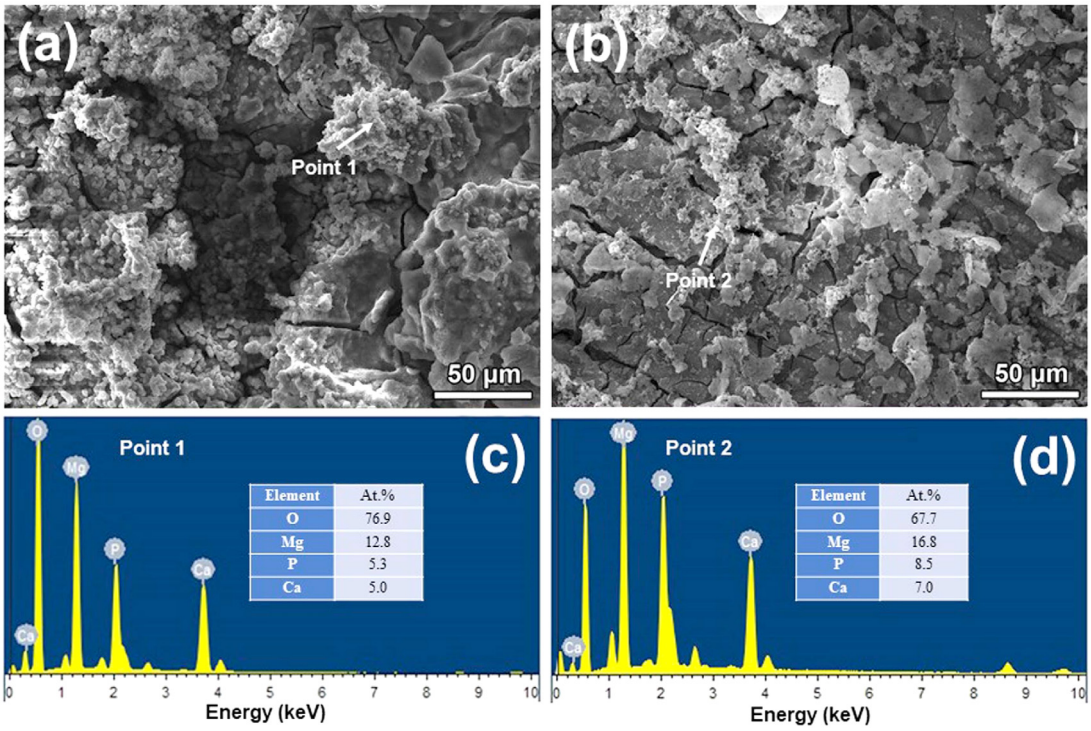

Fig. 28. Typical corrosion morphology and the corresponding EDS results of cast ZK60 (a), (c) and LAMed ZK60 (b), (d) [56].

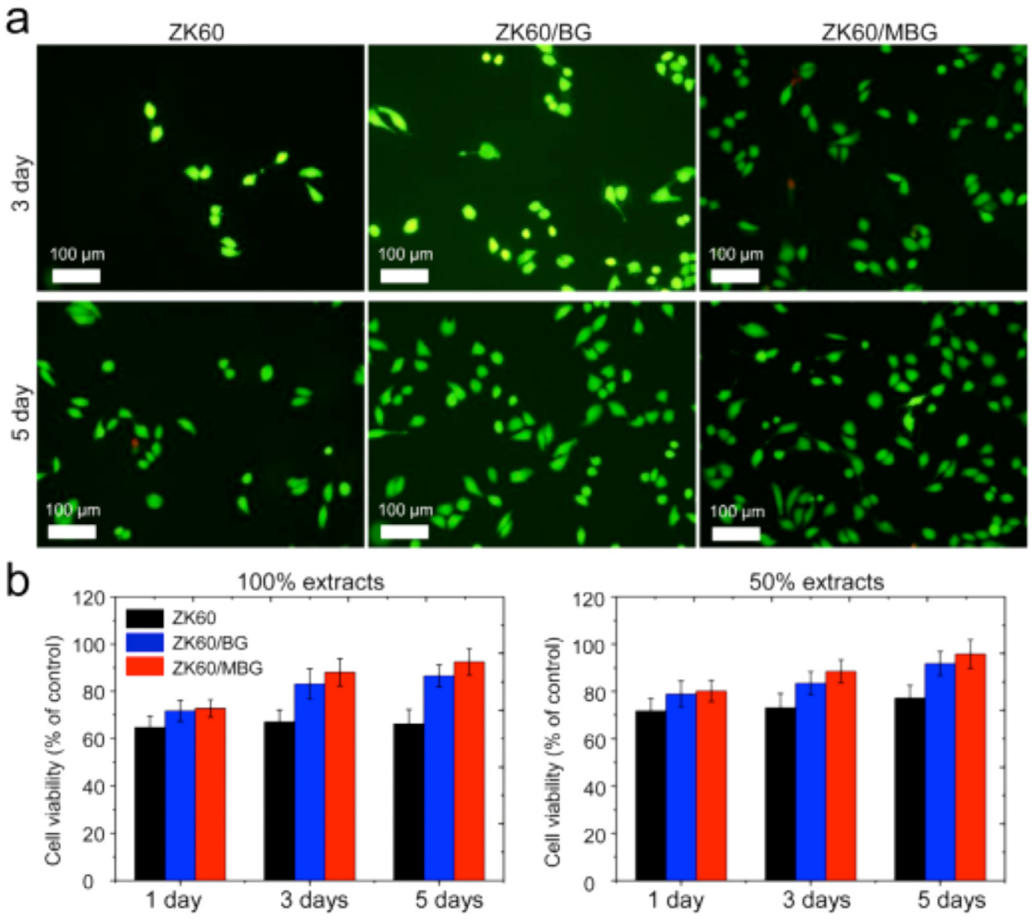

Fig. 29. Biocompatibility of LAMed ZK60, ZK60/BG and ZK60/ mesoporous BG. (a) Live/dead staining images, (b) relative cell viabilities obtained from CCK-8 assays [74].

The corrosion parameters, including corrosion potential, corrosion current density and corrosion rate in simulated body fluid, are summarized in Table 3. It is noticed that the LAMed Mg-based alloys exhibited a comparable or even superior corrosion resistance compared to the samples prepared by traditional processing methods. The increase in corrosion resistance can be attributed to the refined grains and uniform microstructure, which can significantly reduce the fraction of the effective cathodes and restrict microgalvanic coupling resulting from the accumulation of cathodic phases. On the other hand, the solid solubility of alloying elements in Mg-based alloys can be enhanced due to the rapid melting-solidification of LAM, contributing to the formation of more protective and self-healing films. However, it is worth noticing that other factors such as pH, protein and ions concentration can also exert an influence on corrosion in the body environment. Current studies on the biodegradation of LAMed Mg-based alloys are mainly focused on the *in vitro* tests, and no *in vivo* degradation behavior is reported to the best knowledge of the authors.

3.6. Biocompatibility of LAMed Mg-based alloys

Mg is one of the important elements in human body and it takes part in almost all cellular system, membrane function and membrane integrity. It has been reported that the amount of Mg in the human body is approximately 21–28 g and more than half of it is present in bone tissue. Soft tissues possessed 35–40% of this content and less than 1% is found in serum [85]. In addition, Mg^{2+} ions also contribute to the transformation of immature bone to mature bone. Yang et al [60]. evaluated the biocompatibility of LAMed ZK60 and ZK60/BG alloys (Fig. 27), and revealed that very few dead cells were observed on these samples. Cell viability for LAMed ZK60 and ZK60/BG alloys was enhanced with the increase of culture time. In addition, the cells tightly adhered on LAMed ZK60 and ZK60/BG alloys as detected by direct contact method, implying that LAMed samples possessed favorable cell adhesion property. It is also reported from a previous work [56] that the corrosion products of LAMed ZK60 after 7-d immersion in simulated body fluids were mainly composed of O, Mg, P and Ca (Fig. 28), indirectly indicating a good hydroxyapatite-forming ability.

Moreover, Yang et al [74]. introduced mesoporous BG into Mg matrix composite via LAM, and a comparative study on biocompatibility was carried out among the LAMed ZK60, ZK60/BG and ZK60/mesoporous BG (Fig. 29). It is noticed that the cells exhibited typical fusiform shape on ZK60/mesoporous BG, in comparison with round shape

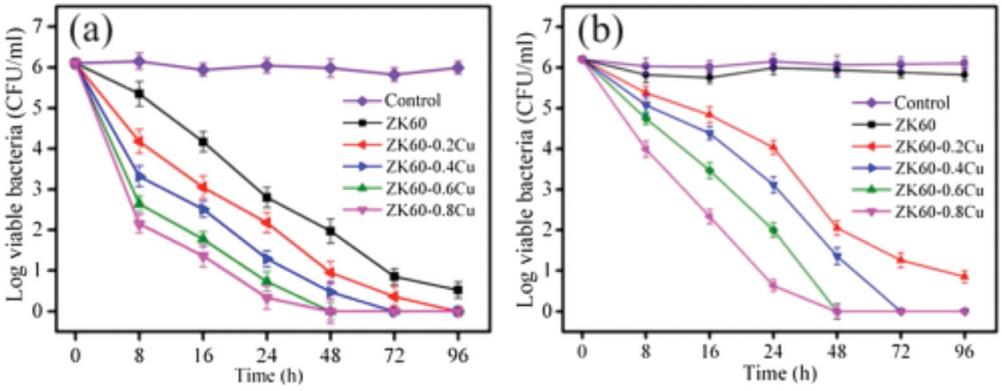

Fig. 30. CFU/mL of Escherichia Coli after incubation in alloy extracts at various immersion time: (a) normal pH values; (b) neutral pH of 7.4 [46].

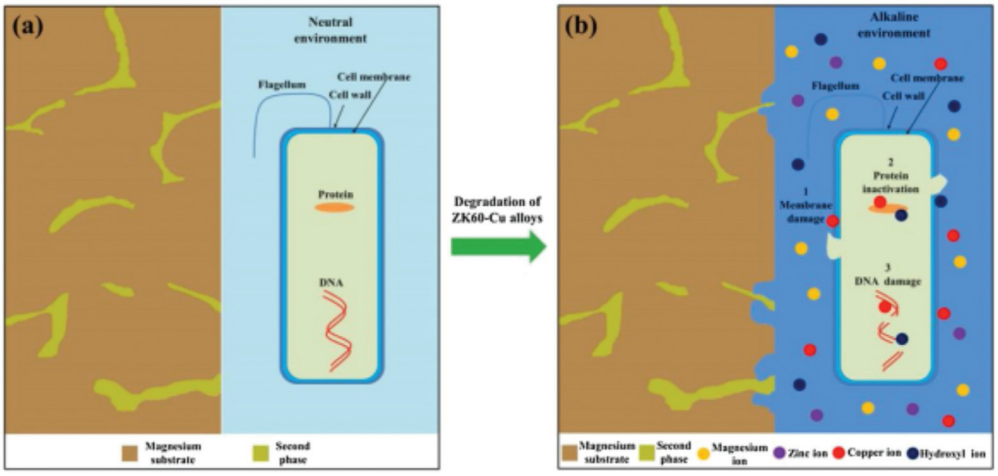

Fig. 31. Antibacterial mechanism for ZK60-Cu alloys in body fluid environment before (a) and after (b) degradation [46].

on ZK60 and ZK60/BG. Meanwhile, there were more cells attached on ZK60/mesoporous BG. The cell viability increased from 91.6% on day 3 to 95.8% on day 5 for ZK60/mesoporous BG, which was higher than that of ZK60 and ZK60/BG. These results indicated that LAMed Mg matrix composites displayed an enhanced biocompatibility.

3.7. Antibacterial property of LAMed Mg-based alloys

Bacterial infection might result in implant loosening or even implantation failure, indicating that it is of great importance to inhibit bacterial-related infections [86,87]. Cu exhibits excellent anti-bacterial ability owing to the positively charged Cu ions released in the body fluids, which can attach to negatively charged bacterial cell wall, perturb membrane permeability, and lead to their lysis and death. In addition, some enzymes can also be inactivated via the reaction between Cu ions and their thiol groups, leading to the death of bacterial cells [47]. Moreover, Cu is an essential trace element for the human body, acting as a catalytic cofactor for many key metabolic enzymes. Xu et al [46]. prepared Cu-containing antibacterial ZK60 alloys by LAM and reported that the LAMed ZK60-Cu alloys possessed strong antibacterial ability (Fig. 30). The antibacterial mechanism for LAMed ZK60-Cu alloys in body fluid environment was analyzed as shown in Fig. 31. It implied that the combined effect of Cu ions and alkaline environment can effectively kill the bacteria through damaging cellular membrane structure, denaturing enzymes and prohibiting deoxyribonucleic acid replication.

4. Biodegradable porous Mg-based alloys by LAM for potential biomedical implant applications

Human bone is porous in structure with three major anatomic cavities of different sizes, and these cavities play an important role in reshaping the processes and mechanical integrity of the bone [88]. Traditional porous biomaterials possess a random distribution of open or closed voids, and the solid surface of metal is very different from the porous nature of human bones. This unavoidably limits the fixation of the implants with the body tissue and also affects the transport of body fluid. In addition, in traditional processing methods, such as casting and powder metallurgy, it is difficult to fabricate porous implants with complex external shapes and intri-

cate internal architectures, particularly in combination with appropriate stiffness and strength. However, the high geometric freedom offered by LAM can be employed to prepare complex implants with interconnected porous structure. Therefore, biodegradable porous Mg-based samples prepared by LAM show a great potential in biomedical implant applications as they can display a fully-interconnected porous structure with periodic cellular lattice, which provides adequate spaces for transportation of nutrients in bone growth while the implants degrade in the human body as the bone regenerates. Li et al [89]. used LAM to prepare biodegradable porous WE43 scaffolds with fully interconnected porous structure, and the scaffolds possessed proper mechanical properties even after 4 weeks of biodegradation and satisfactory biodegradation rate with approximate 20% volume loss after 4 weeks. Nevertheless, the struts exhibited relatively high roughness in the center even after being chemically polished. In addition, the dynamic corrosion behavior and mechanical property still remain unclear. In conclusion, studies on LAM of biodegradable porous Mg-based alloys for biomedical implant applications are still in its infancy.

5. Concluding remarks and future perspectives

This work summarizes the recent progress of LAM of Mg-based alloys. From the processing point of view, LAM of biodegradable Mg-based alloys yields promising results as LAM can tailor-make Mg implants with a desirable degradation rate that are difficult or impossible to achieve by conventional melting or deformation processing. In addition, the rapid development of LAM system for Mg-based alloys has made it easier for preparing parts with geometric complexity and fine structures, including porous structure, at increasing efficiency.

From the point of view of composition selection for Mg-based alloys, researchers are trying to develop biologically safe Mg-based alloys by adding non-toxic elements such as Zn, Mn, Zr, Ca and Li and so on. LAM can fabricate the bulk Mg-based alloys with a moderate corrosion rate, appropriate mechanical properties, good biocompatibility and excellent bio-safety. Nevertheless, in comparation with Fe-based, Ni-based, Ti-based, and Al-based alloys, the studies on LAM of Mg-based alloys are still in its infancy and a considerable amount of work is required before Mg-based alloys prepared by LAM are practically applicable in biomedical fields. First, the window of processing conditions for good formability should be established so that high-quality samples can be achieved routinely and easily. Second, the current studies on the mechanical properties of LAMed Mg-based alloys mainly focus on the hardness tests and few works investigate the tensile properties and compressive properties, while no studies on fatigue tests were reported. In addition, the complex interaction between mechanical and corrosion properties in body fluid environment (corrosion-fatigue) is still absent. Last but not the least, the relationship of processing parameters-composition-microstructure-property is yet to be established to realize high-performance Mg-based alloys by LAM.

Declaration of Competing Interest

The authors declare that they have no known competing financial interests or personal relationships that could have appeared to influence the work reported in this paper.

CRediT authorship contribution statement

C.L. Wu: Investigation, Visualization, Writing – original draft. **W.J. Xie:** Investigation, Writing – original draft. **H.C. Man:** Conceptualization, Funding acquisition, Writing – review & editing, Supervision.

Acknowledgments

The work described in this paper was fully supported by a grant from the Research Grants Council of the Hong Kong Special Administrative Region (152131/18E). Support from the infrastructure of The Hong Kong Polytechnic University is also acknowledged.

References

[1] S. Vazirian, A. Farzadi, J. Alloy. Compd. 829 (2020) 154510.
[2] D.N. Liu, Z.C. Ma, H.W. Zhao, L.Q. Ren, W. Zhang, Mater. Today Commun. 28 (2021) 102659.
[3] E.K. Brooks, R.P. Brooks, M.T. Ehrensberger, Mater. Sci. Eng. C 71 (2017) 200–205.
[4] S. Rajasekar, R. Chetty, L. Neelakantan, Int. J. Hydrog. Energy 40 (2015) 12413–12423.
[5] Y.C. Wu, C.N. Kuo, T.H. Wu, T.Y. Liu, Y.W. Chen, X.H. Guo, J.C. Huang, Mater. Today Commun. 27 (2021) 102346.
[6] A.J. Hart, P.D. Quinn, B. Sampson, A. Sandison, K.D. Atkinson, J.A. Skinner, J.J. Powell, J.F.W. Mosselmans, Acta Biomater. 6 (2010) 4439–4446.
[7] J. Fiocchi, J.N. Lemke, S. Zilio, C.A. Biff, A. Coda, A. Tuissi, Mater. Today Commun. 27 (2021) 102447.
[8] O.T. Adesina, E.R. Sadiku, T. Jamiru, O.S. Adesina, O.F. Ogunbiyi, B.A. Obadele, S. Salifu, J. Mater. Res. Technol. 9 (2020) 11801–11812.
[9] R. Liu, R. He, J. Xiao, M. Tang, H. Zhang, S. Guo, Mater. Lett. 247 (2019) 185–188.
[10] A. Nigam, S. Saini, A.K. Rai, S.J. Pawar, Mater. Today Commun. 28 (2021) 102683 2021.
[11] L. Jin, C.X. Chen, G.Z. Jia, Y.T. Li, J. Zhang, H. Huang, B. Kang, G.Y. Yuan, H. Zeng, T.X. Chen, Acta Biomater. 106 (2020) 428–438.
[12] S. Jin, D. Zhang, X.P. Lu, Y. Zhang, L.L. Tan, Y. Liu, Q. Wang, J. Mater. Sci. Technol. 47 (2020) 190–201.
[13] H. Zhou, B. Liang, H.T. Jiang, Z.L. Deng, K.X. Yu, J. Magnes. Alloy. 9 (2021) 779–804.
[14] M. Zhu, Y.J. Lu, C.K. Zhang, L. Li, M.M. Xie, J.X. Lin, K.L. Tang, Surf. Coat. Technol. 372 (2019) 209–217.
[15] Q. Dong, X. Zhou, Y. Feng, K. Qian, H. Liu, M. Lu, C. Chu, F. Xue, J. Bai, Bioact. Mater. 6 (2021) 158–168.
[16] Y.W. Yang, C.X. He, D.Y. E, W.J. Yang, F.W. Qi, D.Q. Xie, L.D. Shen, S.P. Peng, C.J. Shuai, Mater. Des. 185 (2020) 108259.
[17] M. Knapek, M. Zemková, A. Greš, E. Jablonská, F. Lukác, R. Král, J. Bohlen, P. Minárik, J. Magnes. Alloy. 9 (2021) 853–865.
[18] G. Singh, S. Singh, C. Prakash, S. Ramakrishna, J. Magnes. Alloy. 9 (2021) 1272–1284.
[19] Y.W. Gui, Q.A. Li, K.G. Zhu, Y.B. Xue, Mater. Today Commun. 27 (2021) 102282.
[20] E.P. Silva, R.H. Buzolin, F. Marques, F. Soldera, U. Alfaro, H.C. Pinto, J. Magnes. Alloy. 9 (2021) 995–1006.

[21] X. Chen, D.F. Zhang, J.Y. Xu, J.K. Feng, Y. Zhao, B. Jiang, F.S. Pan, J. Alloy. Compd. 850 (2021) 156711.
[22] V.E. Bazhenov, A.V. Li, A.A. Komissarov, A.V. Koltygin, S.A. Tavolzhanskii, V.A. Bautin, O.O. Voropaeva, A.M. Mukhametshina, A.A. Tokar, J. Magnes. Alloy. 9 (2021) 1428–1442.
[23] J. Chen, L. Tan, K. Yang, Bioact. Mater. 2 (2017) 19–26.
[24] Y. Sun, B. Zhang, Y. Wang, L. Geng, X. Jiao, Mater. Des. 34 (2012) 58–64.
[25] Y. Song, E.H. Han, D. Shan, C.D. Yim, B.S. You, Corros. Sci. 60 (2012) 238–245.
[26] L. Wei, J. Li, Y. Zhang, H. Lai, Mater. Chem. Phys. 241 (2020) 122441.
[27] E. Zhang, D. Yin, L. Xu, L. Yang, K. Yang, Mater. Sci. Eng. C 29 (2009) 987–993.
[28] J.X. Tao, M.C. Zhao, Y.C. Zhao, D.F. Yin, L. Liu, C.D. Gao, C.J. Shuai, A. Atrens, J. Magnes. Alloy. 8 (2020) 952–962.
[29] C.C. Ng, M.M. Savalani, H.C. Man, I. Gibson, Virtual Phys. Prototyp. 5 (2010) 13–19.
[30] C.D. Gao, S. Li, L. Liu, S.Z. Bin, Y.W. Yang, S.P. Peng, C.J. Shuai, J. Magnes. Alloy. 9 (2021) 305–316.
[31] C.L. Wu, S. Zhang, C.H. Zhang, J.B. Zhang, Y. Liu, J. Chen, Opt. Laser Technol. 115 (2019) 134–139.
[32] M. Katancik, S. Mirzababaei, M. Ghayoor, S. Pasebani, J. Alloy. Compd. 849 (2020) 156319.
[33] Z.J. Li, X.N. Gu, S.Q. Lou, Y.F. Zheng, Biomaterials 29 (2008) 1329–1344.
[34] X.N. Gu, N. Li, Y.F. Zheng, L.Q. Ruan, Mater. Sci. Eng. B 176 (2011) 1778–1784.
[35] C.J. Shuai, Y.W. Yang, P. Wu, X. Lin, Y. Liu, Y.Z. Zhou, P. Feng, X.Y. Liu, S.P. Peng, J. Alloy. Compd. 691 (2017) 961–969.
[36] G.R. Argade, S.K. Panigrahi, R.S. Mishra, Corros. Sci. 58 (2012) 145–151.
[37] X. Zhao, Y.H. Lv, S.Y. Dong, S.X. Yan, X.T. Liu, Y.X. Liu, P. He, T.S. Lin, B.S. Xu, H.S. Han, Opt. Laser Technol. 132 (2020) 106487.
[38] J.S. Jesus, L.P. Borrego, J.A.M. Ferreira, J.D. Costa, C. Capela, Eng. Fail. Anal. 118 (2020) 104852.
[39] A.R. Balachandramurthi, N.R. Jaladurgam, C. Kumara, T. Hansson, J. Moverare, J. Gardstam, R. Pederson, Materials 13 (2020) 5198.
[40] M.S. Kenevisi, F. Lin, J. Alloy. Compd. 843 (2020) 155866.
[41] C.C. Ng, M.M. Savalani, H.C. Man, I. Gibson, Virtual Phys. Prototyp. 2 (2010) 13–19.
[42] D. Hu, Y. Wang, D.F. Zhang, L. Hao, J.J. Jiang, Z.H. Li, Y.T. Chen, Mater. Manuf. Process. 30 (2015) 1298–1304.
[43] D. Wang, Y.Q. Yang, Y.L. Huang, W.H. Wu, T.T. Sun, X.R. He, Laser Technol. 34 (2010) 447–451.
[44] K. Wei, Z. Wang, X. Zeng, Mater. Lett. 156 (2015) 187–190.
[45] X. Niu, H. Shen, J. Fu, Mater. Lett. 221 (2018) 4–7.
[46] R. Xu, M.C. Zhao, Y.C. Zhao, L. Liu, C. Liu, C. Gao, C. Shuai, A. Atrens, Mater. Lett. 237 (2019) 253–257.
[47] C. Shuai, L. Liu, M. Zhao, P. Feng, Y. Yang, W. Guo, C. Gao, F. Yuan, J. Mater. Sci. Technol. 34 (2018) 1944–1952.
[48] K. Wei, M. Gao, Z. Wang, X. Zeng, Mater. Sci. Eng. A 611 (2014) 212–222.
[49] H. Liao, P. Fu, L. Peng, J. Li, S. Zhang, G. Hu, W. Ding, Mater. Sci. Eng. A 687 (2017) 281–287.
[50] C. Liu, M. Zhang, C. Chen, Mater. Sci. Eng. A 703 (2017) 359–371.
[51] K. Wei, X. Zeng, Z. Wang, J. Deng, M. Liu, G. Huang, X. Yuan, Mater. Sci. Eng. A 756 (2019) 226–236.
[52] N.A. Zumdick, L. Jauer, L.C. Kersting, T.N. Kutz, J.H. Schleifenbaum, D. Zander, Mater. Charact. 147 (2019) 384–397.
[53] C. Shuai, C. He, P. Feng, W. Guo, C. Gao, P. Wu, Y. Yang, S. Bin, Virtual Phys. Prototyp. 13 (2018) 59–69.
[54] C. Shuai, C. He, L. Xu, Q. Li, T. Chen, Y. Yang, S. Peng, Virtual Phys. Prototyp. 13 (2018) 292–300.
[55] B.C. Zhang, H.L. Liao, C. Coddet, Mater. Des. 34 (2012) 753–758.
[56] C.L. Wu, W. Zai, H.C. Man, Mater. Today Commun. 26 (2021) 101922.
[57] D.S. Watring, J.T. Benzing, N. Hrabe, A.D. Spear, Addit. Manuf. 36 (2020) 101425.
[58] S. Zhang, C.L. Wu, C.H. Zhang, Mater. Lett. 141 (2015) 7–9.
[59] A.D. Plessis, Addit. Manuf. 30 (2019) 100871.
[60] Y. Yang, C. Lu, S. Peng, L. Shen, D. Wang, F. Qi, C. Shuai, Virtual Phys. Prototyp. 15 (2020) 278–293.
[61] Y.W. Yang, P. Wu, X. Lin, Y. Liu, H. Bian, Y.Z. Zhou, C.D. Gao, C.J. Shuai, Virtual Phys. Prototyp. 11 (2016) 173–181.
[62] H. Zhu, L. Lu, J.Y.H. Fuh, Proc. Inst. Mech. Eng. Part B 220 (2006) 183–190 Journal of Engineering Manufacture.
[63] W.L. Wang, D. Wang, L. He, W.Q. Liu, X. Yang, Mater. Res. Express. 7 (2020) 116519.
[64] X.N. Gu, W.R. Zhou, Y.F. Zheng, Y. Cheng, S.C. Wei, S.P. Zhong, T.F. Xi, L.J. Chen, Acta Biomater. 6 (2010) 4605–4613.
[65] L. Liu, H.T. Ma, C.D. Gao, C.J. Shuai, S.P. Peng, J. Alloy. Compd. 835 (2020) 155397.
[66] Z. Panahi, E. Tamjid, M. Rezaei, Surf. Coat. Technol. 386 (2020) 125461.
[67] M. Uddin, C. Hall, V. Santos, R. Visalakshan, G. Qian, K. Vasilev, Mater. Sci. Eng. C 118 (2021) 111459.
[68] S. Zaichick, V. Zaichick, V. Karandashev, S. Nosenko, Metallomics 3 (2011) 186–194.
[69] H. Li, H. Yang, Y. Zheng, F. Zhou, K. Qiu, X. Wang, Mater. Des. 83 (2015) 95–102.
[70] M. Sabbaghian, R. Mahmudi, K.S. Shin, Mater. Sci. Eng. A 792 (2020) 139828.
[71] G.N. Li, S.M. Zhu, J.F. Nie, Y. Zheng, Z. Sun, Bioact. Mater. 6 (2021) 1468–1478.
[72] P.C. Lin, K.F. Lin, C. Chiu, V.I. Semenov, H.C. Lin, M.J. Chen, Surf. Coat. Technol. 427 (2021) 127811.
[73] J. Huang, Y. Ren, Y. Jiang, B. Zhang, K. Yang, Front. Mater. Sci. China 1 (2007) 405–409.
[74] Y.W. Yang, C.F. Lu, L.D. Shen, Z.Y. Zhao, S.P. Peng, C.J. Shuai, J. Magnes. Alloy. (2021), doi:10.1016/j.jma.2021.04.009.
[75] Y. Yin, Q.L. Huang, L.X. Liang, X.B. Hu, T. Liu, Y.Z. Weng, T. Long, Y. Liu, Q.X. Li, S.Q. Zhou, H. Wu, J. Alloy. Compd. 785 (2019) 38–45.
[76] A. Hidouci, J.M. Pelletier, F. Ducoin, D. Dezert, R.E. Guerjouma, Surf. Coat. Technol. 123 (2000) 17–23.
[77] H. Okamoto, J. Phase Equilib. 15 (1994) 129–130.
[78] B. Manne, H. Thiruvayapati, S. Bontha, R.M. Rangarasaiah, M. Das, V.K. Balla, Surf. Coat. Technol. 347 (2018) 337–349.
[79] H.L. Ding, L.F. Liu, S. Kamado, W.J. Ding, Y. Kojima, J. Alloy. Compd. 456 (2008) 400–406.
[80] Y. Lu, A.R. Bradshaw, Y.L. Chiu, I.P. Jones, J. Alloy. Compd. 614 (2014) 345–352.
[81] R. Willumeit, J. Fischer, F. Feyerabend, N. Hort, U. Bismayer, S. Heidrich, B. Mihailova, Acta Biomater. 7 (2011) 2704–2715.
[82] M. Alvarez-Lopez, M.D. Pereda, J.A. del Valle, M. Fernandez-Lorenzo, M.C. Garcia-Alonso, O.A. Ruano, M.L. Escudero, Acta Biomater. 6 (2010) 1763–1771.
[83] C.H. Cai, R.B. Song, L.X. Wang, J.Y. Li, Appl. Surf. Sci. 462 (2018) 243–254.
[84] D. Hong, P. Saha, D.T. Chou, B. Lee, B.E. Collins, Z.Q. Tan, Z.Y. Dong, P.N. Kumta, Acta Biomater. 9 (2013) 8534–8547.
[85] J. Walker, S. Shadanbaz, T.B.F. Woodfield, M.P. Staiger, G.J. Dias, J. Biomed. Mater. Res. 102 (2014) 1316–1331.
[86] E. Zhang, F. Li, H. Wang, J. Liu, C. Wang, M. Li, K. Yang, Mater. Sci. Eng. C 33 (2013) 4280–4287.
[87] M.H. Wong, H.C. Man, Mater. Lett. 229 (2018) 229–231.
[88] X. Wang, Q. Ni, J. Orthop. Res. 21 (2003) 312–319.
[89] Y. Li, J. Zhou, P. Pavanram, M.A. Leeflang, L.I. Fockaert, B. Pouran, N. Tümer, K.U. Schröder, J.M.C. Mol, H. Weinans, H. Jahr, A.A. Zadpoor, Acta Biomater. 67 (2018) 378–392.